Antiprotons in cosmic rays from neutralino annihilation

F. Donato,[1,*] N. Fornengo,[1,2,†] D. Maurin,[3,‡] P. Salati,[4,§] and R. Taillet[4,‖]
[1]*Dipartimento di Fisica Teorica, Università di Torino, Istituto Nazionale di Fisica Nucleare, Sezione di Torino, Via P. Giuria 1, I–10125 Torino, Italy*
[2]*School of Physics, Korea Institute for Advanced Study, 207-43 Cheongryangri-dong, Dongdaemun-gu, Seoul 130-012, Korea*
[3]*Service d'Astrophysique, SAp CEA-Saclay, F-91191 Gif-sur-Yvette CEDEX, France*
[4]*Laboratoire de Physique Théorique LAPTH, Annecy-le-Vieux, 74941, France and Université de Savoie, Chambéry, 73011, France*
(Received 10 June 2003; published 2 March 2004)

We calculate the antiproton flux due to relic neutralino annihilations, in a two-dimensional diffusion model compatible with stable and radioactive cosmic ray nuclei. We find that the uncertainty in the primary flux induced by the propagation parameters alone is about two orders of magnitude at low energies, and it is mainly determined by the lack of knowledge of the thickness of the diffusive halo. On the contrary, different dark matter density profiles do not significantly alter the flux: a Novarro-Frenk-White distribution produces fluxes which are at most 20% higher than an isothermal sphere. The most conservative choice for propagation parameters and dark matter distribution normalization, together with current data on cosmic antiprotons, cannot lead to any definitive constraint on the supersymmetric parameter space, either in a low-energy effective minimal supersymmetric standard model, or in a minimal supergravity scheme. However, if the best choice for propagation parameters—corresponding to a diffusive halo of $L=4$ kpc—is adopted, some supersymmetric configurations with the neutralino mass $m_\chi \lesssim 100$ GeV should be considered as excluded. An enhancement flux factor—due for instance to a clumpy dark halo or a higher local dark matter density—would imply a more severe cut on the supersymmetric parameters.

DOI: 10.1103/PhysRevD.69.063501 PACS number(s): 95.35.+d, 96.40.−z, 98.35.Gi, 98.35.Pr

I. INTRODUCTION

The recent Wilkinson Microwave Anisotropy Probe (WMAP) measurements of the cosmic microwave background (CMB) anisotropies [1] point toward a flat universe with a fraction $\Omega_\Lambda \simeq 0.7$ of the closure density in the form of a negative pressure component—such as a cosmological constant or a scalar field—while the remaining $\Omega_m \simeq 0.3$ is matter. These conclusions are independently reached from the determination of the relation between the luminosity distance and the redshift of supernovas of type Ia (SNIa) [2] on the one hand and from the large scale structure information from galaxy and cluster surveys [3]. The WMAP values of $\Omega_m = 0.27 \pm 0.04$ and $\Omega_B = 0.044 \pm 0.004$ indicate that most of the matter is nonbaryonic. The amount of baryonic matter Ω_B deduced from the CMB is in perfect agreement with the results from primordial nucleosynthesis and observations of the deuterium abundance in quasar absorption lines [4].

The nature of this astronomical dark matter has been challenging physicists for several decades and is still unresolved. The favored candidate is a weakly interacting massive particle. The so-called neutralino naturally arises in the framework of supersymmetric theories as the lightest combination of neutral Higgsinos and gauginos. A great deal of effort has been devoted to pinning down these evading species [5]. Experimental techniques [6–8] have been devised in order to be sensitive to the recoil energy which a neutralino may deposit as it crosses a terrestrial detector. The annihilation photons from the neutralinos that populate the Milky Way halo [9] or extragalactic systems [10] are under scrutiny. As a matter of fact, a gamma-ray excess has been recently reported by HEGRA in the direction of the giant elliptical M87 [11]. Antimatter cosmic-ray particles are also expected from neutralino annihilations inside our galaxy. A subtle feature in the positron spectrum has actually been measured by the HEAT Collaboration [12] for energies beyond 7 GeV.

This work is devoted to cosmic-ray antiprotons whose energy spectrum has already been measured with some accuracy. Much larger statistics will soon be collected by the AMS Collaboration on board the International Space Station (ISS) by the BESS-Polar long duration balloon experiment and by the PAMELA satellite. Secondary antiprotons are naturally produced by the spallation of primary nuclei—mostly cosmic-ray protons and helions—on the diffuse gas of the Milky Way ridge. If neutralinos pervade our galaxy, a primary component adds up to that secondary distribution. The spectral distortion that ensues is expected *a priori* in the low-energy region for merely kinematic reasons [13]: unlike for a neutralino annihilation, the center-of-mass frame of a spallation event is not at rest with respect to the galaxy. In principle, an excess of low-energy antiprotons is the signature of an unconventional production—either neutralino annihilation or small black hole evaporation [14] for instance. However, because antiprotons undergo inelastic yet nonannihilating collisions with the interstellar material, the high-energy particles tend to lose energy and to populate the low-energy tail of the spectrum, which consequently is much flatter [15] than previously estimated. This motivated the search for other cosmic-ray signatures such as antideuterons

*Electronic address: donato@to.infn.it
†Electronic address: fornengo@to.infn.it
‡Electronic address: dmaurin@cea.fr
§Electronic address: salati@lapp.in2p3.fr
‖Electronic address: taillet@lapp.in2p3.fr

[16,17]. Antiproton production from primary cosmic-ray spallations is the natural background to any unconventional excess that would signal, for instance, the presence of the putative neutralinos. The detailed calculation of that secondary component [18] has required the determination of the propagation-diffusion parameters that are consistent with the B/C data [19]. By varying those parameters over the entire range allowed by the cosmic-ray nuclei measurements, the theoretical uncertainty on the antiproton secondary flux has been found to be 9% from 100 MeV to 1 GeV. It reaches a maximum of 24% at 10 GeV and decreases to 10% at 100 GeV. This small scatter in the secondary antiproton spectrum is not surprising. Cosmic-ray nuclei such as LiBeB and secondary antiprotons are both manufactured in the same place—the interstellar gas of the galactic disk—through the same production mechanism—the spallation of primaries.

The aim of this article is to calculate the supersymmetric cosmic-ray antiproton flux that arise from the diffusion-propagation parameter space and to estimate the uncertainties due to its spread. Since neutralinos annihilate all over the Milky Way and are not confined to the disk alone, we anticipate that the uncertainty in that primary component will be much larger than for secondaries.

The discussion will be split into two main directions, brought to the fore by the structure of the equation describing the primary flux. Production and propagation may be disentangled in the limit where the energy does not change as antiprotons travel. That is not strictly correct, as diffusive reacceleration as well as adiabatic and Coulomb losses generate a diffusion in energy space that is discussed in Appendix. The elementary process of supersymmetric antiproton production through neutralino annihilation is discussed in Sec. II, both in an effective minimal supersymmetric standard model (MSSM) and in a supergravity-inspired model. The two-zone propagation-diffusion model and the dependence of the primary antiproton flux $\Phi_{\bar{p}}^{\mathrm{SUSY}}$ on the propagation parameters are described in Sec. III. The thickness L of the magnetic halo is naively expected to be the dominant source of uncertainty for $\Phi_{\bar{p}}^{\mathrm{SUSY}}$ as the larger the confinement layers, the larger the fiducial volume where neutralino annihilations take place, and the larger the supersymmetric antiproton flux. Actually, L is combined with the diffusion coefficient $K(E)$ and the galactic wind velocity V_c in order to get a precise value for the B/C ratio and for the antiproton flux. We present the results for the primary flux in Sec. IV, where we estimate the uncertainties induced by the spread of the diffusion-propagation parameter space. We also briefly discuss the modifications of $\Phi_{\bar{p}}^{\mathrm{SUSY}}$ due to different choices in the dark matter distribution function, in its normalization, and in the core radius values. In Sec. V, the comparison of the latest antiproton measurements with the antiproton fluxes predicted in different supersymmetric schemes will be discussed as a function of the propagation-diffusion parameters and of the neutralino galactic distribution. Conclusions and perspectives will be presented in Sec. VI.

II. THE NEUTRALINO-INDUCED ANTIPROTONS: THE SOURCE TERM

Antiprotons can be produced by self-annihilation of neutralinos in the galactic halo. Dark matter neutralinos may be considered almost at rest in the galactic frame since their average velocity is of the order of 300 $\mathrm{km\,s^{-1}}$. They are therefore highly nonrelativistic. The production differential rate per unit volume and time is a function of space coordinates (r,z defined in the galactic rest frame) and antiproton kinetic energy $T_{\bar{p}}$. It is defined as

$$q_{\bar{p}}^{\mathrm{SUSY}}(r,z,T_{\bar{p}}) = \langle \sigma_{\mathrm{ann}} v \rangle_0 g(T_{\bar{p}}) \left(\frac{\rho_\chi(r,z)}{m_\chi} \right)^2, \qquad (1)$$

where $\langle \sigma_{\mathrm{ann}} v \rangle_0$ denotes the average over the galactic velocity distribution function of the neutralino pair annihilation cross section σ_{ann} multiplied by the relative velocity v, m_χ is the neutralino mass, and $\rho_\chi(r,z)$ is the mass distribution function of neutralinos inside the galactic halo. Since relic neutralinos behave as cold dark matter, their distribution has to follow the matter density profile $\rho_{\mathrm{DM}}(r,z)$ of the galactic halo:

$$\rho_\chi(r,z) = \xi \rho_{\mathrm{DM}}(r,z), \qquad (2)$$

where ξ parameterizes the fact that the dark halo may not be totally made of relic neutralinos ($\xi \leqslant 1$). This would be the case when neutralinos are not responsible for the total amount of dark matter in the Universe, i.e., when their relic abundance $\Omega_\chi h^2$ is much smaller than the measured value for $\Omega_{\mathrm{DM}} h^2$. This is a situation that occurs in many supersymmetric models. It is reasonable to assume that ξ has no space dependence and that it is related to the relative amount of $\Omega_\chi h^2$ with respect to $\Omega_{\mathrm{DM}} h^2$. We will assume the standard definition

$$\xi = \min(1, \Omega_\chi h^2 / 0.05), \qquad (3)$$

where we have considered that neutralinos with $\Omega_\chi h^2 < 0.05$ cannot be the dominant dark matter component.

Finally, the second term in Eq. (1), $g(T_{\bar{p}})$, denotes the antiproton differential spectrum per annihilation event, defined as

$$g(T_{\bar{p}}) \equiv \frac{1}{\sigma_{\mathrm{ann}}} \frac{d\sigma_{\mathrm{ann}}(\chi\chi \to \bar{p} + X)}{dT_{\bar{p}}} = \sum_F \mathrm{BR}(\chi\chi \to \mathrm{F}) \left(\frac{dN_{\bar{p}}^F}{dT_{\bar{p}}} \right), \qquad (4)$$

where F lists the $\chi\chi$ annihilation final-state particles which can subsequently produce antiprotons either directly (hadronization when $F =$ quarks or gluons), or through subsequent decay of F into quarks or gluons, $\mathrm{BR}(\chi\chi \to \mathrm{F})$ is the branching ratio for the production of F, and $dN_{\bar{p}}^F/dT_{\bar{p}}$ denotes the differential energy distribution of the antiprotons generated by F. For details of the calculation of $g(T_{\bar{p}})$, see Appendix A and Ref. [20].

The source term $q_{\bar{p}}^{\mathrm{SUSY}}(r,z,T_{\bar{p}})$ is therefore a combination of astrophysical factors (the dark matter density profile of the galactic halo) and of particle physics properties (the neutralino self-annihilation cross section and the hadronization into antiprotons of the neutralino annihilation products). The astrophysical and particle physics quantities are factored out and can be studied separately. With the definitions given above, we can rewrite the antiproton source term as

$$q_{\bar{p}}^{\mathrm{SUSY}}(r,z,T_{\bar{p}}) = \Upsilon g(T_{\bar{p}}) \rho_{\mathrm{DM}}^2(r,z) \tag{5}$$

where we have defined the supersymmetric flux factor Υ as

$$\Upsilon = \xi^2 \frac{\langle \sigma_{\mathrm{ann}} v \rangle_0}{m_\chi^2}, \tag{6}$$

which entirely depends on properties of supersymmetric models.

We move now to discuss each term separately.

A. The galactic distribution of dark matter

For most of our discussion, we will assume that the dark matter density distribution is described by a cored isothermal sphere. In terms of the radial distance r in the galactic plane and of the vertical coordinate z, the density profile is

$$\rho_{\mathrm{DM}}(r,z) = \rho_l \frac{a^2 + R_\odot^2}{a^2 + r^2 + z^2}, \tag{7}$$

where a denotes the core radius of the dark halo and $R_\odot$ is the distance of the Sun from the galactic center. We have set $a = 3.5$ kpc and the IAU-recommended value $R_\odot = 8.5$ kpc. The value ρ_l for the total local dark matter density is determined by taking into account the contribution given by the matter density of Eq. (7) to the local rotational velocity v_{rot} [21]. The value of ρ_l compatible with observations ranges from 0.18 GeV cm^{-3} (for a low value of the rotational velocity, $v_{\mathrm{rot}} = 170$ km s^{-1}, and a nonmaximal dark halo) to 0.71 GeV cm^{-3} (for $v_{\mathrm{rot}} = 270$ km s^{-1} and a maximal dark halo) [21]. The interval relative to the preferred value for the rotational velocity ($v_{\mathrm{rot}} = 220$ km s^{-1}) is $0.30\ \mathrm{GeV\,cm^{-3}} \lesssim \rho_l \lesssim 0.47\ \mathrm{GeV\,cm^{-3}}$ [21]. Our results will be presented for $\rho_l = 0.3$ GeV cm^{-3}. Since in the primary antiproton flux ρ_l^2 enters as a pure normalization factor, the fluxes obtained for different values of ρ_l are easily rescaled. For instance, for $\rho_l = 0.47$ GeV cm^{-3}, the antiproton fluxes would be a factor of 2.45 higher than the corresponding ones for $\rho_l = 0.3$ GeV cm^{-3}.

We will come back to the topic of the dark matter density profile at the end of the paper, in Sec. IV B.

B. Supersymmetric models

The existence of a relic particle in supersymmetric theories arises from the conservation of a symmetry, R parity, which prevents the lightest of all the superpartners from decaying. The nature and the properties of this particle depend on the way supersymmetry is broken. The neutralino can be the dark matter candidate in models where supersymmetry is broken through gravity- (or anomaly-)mediated mechanisms. The actual implementation of a specific supersymmetric scheme depends on a number of assumptions on the structure of the model and on the relations among its parameters. This induces a large variability of the phenomenology of neutralino dark matter. In this paper we will consider neutralino dark matter in two different supersymmetric schemes: a low-energy effective-theory implementation of the minimal supersymmetric standard model (EMSSM) and a minimal supergravity model (MSUGRA).

The EMSSM is defined as an implementation of supersymmetry directly at the electroweak scale, which is where the phenomenology of neutralino dark matter is actually studied. The large number of free parameters is reduced by a set of assumptions which are sufficient to shape the properties of the model at the electroweak scale. All the relevant parameters, which set the mass scales and couplings of all the supersymmetric particles (and of the Higgs sector) are taken into account. The free parameters are the gaugino mass parameter M_2, the Higgs boson mixing parameters μ, the ratio of the two Higgs boson vacuum expectation values $\tan\beta$, the mass of the pseudoscalar Higgs boson m_A, a common soft scalar mass for the squarks $m_{\tilde{q}}$, a common soft scalar mass for the sleptons $m_{\tilde{l}}$, and a common dimensionless trilinear parameter A for the third family ($A_{\tilde{b}} = A_{\tilde{t}} \equiv A m_{\tilde{q}}$ and $A_{\tilde{\tau}} \equiv A m_{\tilde{l}}$; the trilinear parameters for the other families are set equal to zero). We assume the standard grand unification relation between the $U(1)$ and $SU(2)$ gaugino mass parameters: $M_1 = 5/3 \tan^2\theta_W M_2$. The parameters will be varied in the following intervals: $100\ \mathrm{GeV} \leqslant M_2 \leqslant 1000$ GeV, $100\ \mathrm{GeV} \leqslant |\mu| \leqslant 1000$ GeV, $100\ \mathrm{GeV} \leqslant m_A \leqslant 1000$ GeV, $100\ \mathrm{GeV} \leqslant m_{\tilde{q}}, m_{\tilde{l}} \leqslant 3000$ GeV, $1 \leqslant \tan\beta \leqslant 50$, and $-3 \leqslant A \leqslant 3$.

A different approach is to embed supersymmetry in a supergravity scheme with boundary conditions at some critical high-energy scale, such as the grand unification (GUT) scale, and keep the number of free parameters and assumptions minimal. This is our MSUGRA. In this class of models we consider gauge coupling constant unification at the GUT scale. In addition, all the mass parameters in the supersymmetric breaking sector are universal at the same GUT scale. The low-energy sector of the model is obtained by evolving all the parameters through renormalization group equations from the GUT scale down to the electroweak scale: this process also induces the breaking of the electroweak symmetry in a radiative way. This model is very predictive, since it relies on only very few free parameters, but at the same time it has a very constrained phenomenology at low energy. It also appears to be quite sensitive to some standard model parameters, like the mass of the top and bottom quarks (m_t and m_b) and the strong coupling constant α_s. In this class of models there are four free parameters: the universal gaugino mass parameter $M_{1/2}$ at the GUT scale, the universal soft scalar mass parameter for both the sfermions and the Higgs bosons m_0 at the GUT scale, a common trilinear coupling for the third family at the GUT scale A_0, and $\tan\beta$. The parameters will be varied in the following intervals: $50\ \mathrm{GeV} \leqslant M_{1/2} \leqslant 1000$ GeV, $0 \leqslant m_0 \leqslant 3000$ GeV, $1 \leqslant \tan\beta \leqslant 50$, and

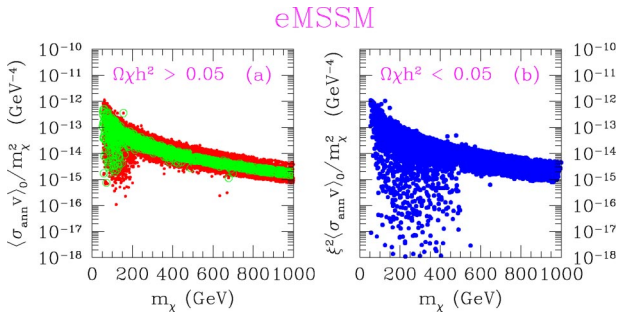

FIG. 1. (Color online) Scatter plot of the supersymmetric flux factor $\Upsilon \equiv \xi^2 \langle \sigma_{\rm ann} v \rangle_0 / m_\chi^2$ as a function of the neutralino mass m_χ, calculated in the EMSSM. (a) refers to supersymmetric configurations with the neutralino as a dominant dark matter component (i.e., $0.05 \leqslant \Omega_\chi h^2 \leqslant 0.3$, and therefore a rescaling factor $\xi = 1$). The light (green) circles show the EMSSM configurations for which the neutralino relic abundance lies in the preferred range for cold dark matter (CDM), as determined by the combined WMAP $+2$DFGRS$+$Lyman-α analysis: $0.095 \leqslant \Omega_{\rm CDM} h^2 \leqslant 0.131$ [1]. (b) refers to the neutralino as a subdominant dark matter particle ($\Omega_\chi h^2 < 0.05$).

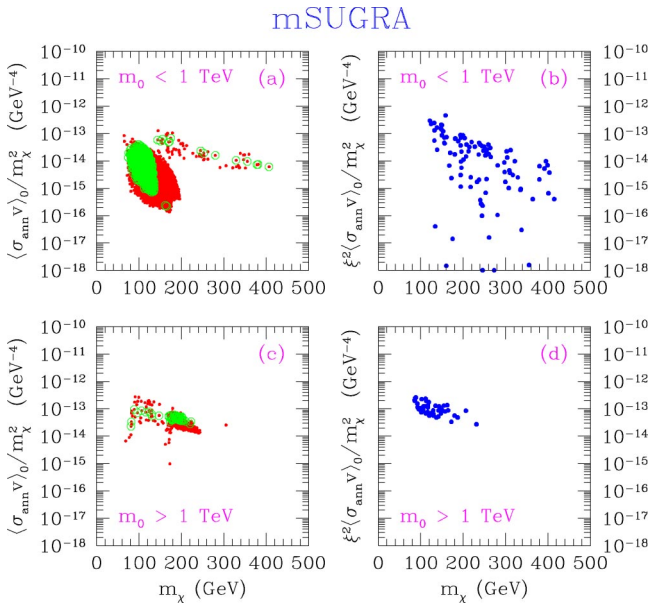

FIG. 2. (Color online) The same as in Fig. 1, calculated in the MSUGRA scheme. (a) and (c) refer to cosmologically dominant neutralinos ($0.05 \leqslant \Omega_\chi h^2 \leqslant 0.3$); (b) and (d) to subdominant neutralinos ($\Omega_\chi h^2 < 0.05$). The upper row (a) and (b) is obtained for the universal soft scalar mass m_0 smaller than 1 TeV (for these models, the neutralino is mostly a Bino state); the lower row (c) and (d) refers to values of m_0 in excess of 1 TeV (in this case the neutralino may have a substantial Higgsino component). The light (green) circles in (a) and (c) show the MSUGRA configurations for which the neutralino relic abundance lies in the preferred range for CDM, as determined by the combined WMAP$+$2DFGRS $+$Lyman-α analysis: $0.095 \leqslant \Omega_{\rm CDM} h^2 \leqslant 0.131$ [1].

$-3 \leqslant A_0 \leqslant 3$. The standard model parameters m_t, m_b, and α_s are varied inside their 2σ allowed ranges.

C. The supersymmetric flux factor Υ

The flux factor Υ defined in Eq. (6) acts as a normalization factor for the antiproton flux and is a purely supersymmetric term. It depends on the mass and couplings of neutralinos in the supersymmetric framework under study. In Fig. 1 we show the flux factor as a function of the neutralino mass for a scan of the EMSSM. Figure 2 reports the case for the MSUGRA scheme. We show the values of Υ separately for the case of comsologically dominant [$0.05 \leqslant \Omega_\chi h^2 \leqslant 0.3$, Fig. 1(a) and Figs. 2(a) and 2(c)] and subdominant [$\Omega_\chi h^2 < 0.05$, Fig. 1(b) and Figs. 2(b) and 2(d)] relic neutralinos. Among the cosmologically relevant ones, we also show the configurations that yield $\Omega_\chi h^2$ inside the preferred range for CDM, as determined by the combined WMAP $+2$DFGRS$+$Lyman-α analysis: $0.095 \leqslant \Omega_{\rm CDM} h^2 \leqslant 0.131$ [1]. The results in the EMSSM show that the upper values of Υ are around 10^{-12} GeV^{-4} for neutralino masses close to the experimental lower bound (around 50 GeV) and then decrease below 10^{-14} GeV^{-4} for $m_\chi \sim 1$ TeV.

In the case of dominant relic neutralinos, the interval of values for Υ is restricted, at all masses: in order to have values of $\Omega_\chi h^2$ that fall in the cosmologically relevant range, the annihilation cross section integrated from freeze-out down to the present time must be inside the interval 3×10^{-11} GeV$^{-2} \lesssim \langle \sigma_{\rm ann} v \rangle_{\rm int} \lesssim 2 \times 10^{-10}$ GeV^{-2}. We recall that the relic abundance depends on $\langle \sigma_{\rm ann} v \rangle_{\rm int}$ ($\Omega_\chi h^2 \propto \langle \sigma_{\rm ann} v \rangle_{\rm int}^{-1}$). This cross section, due to the nonvanishing temperature in the early Universe, may differ quite substantially from the zero-temperature cross section $\langle \sigma_{\rm ann} v \rangle_0$, which is instead relevant for the antiproton signal. Usually a correlation between $\langle \sigma_{\rm ann} v \rangle_{\rm int}$ and $\langle \sigma_{\rm ann} v \rangle_0$ is present when the zero-temperature $\langle \sigma_{\rm ann} v \rangle_0$ is large; on the contrary, when $\langle \sigma_{\rm ann} v \rangle_0$ is small, temperature corrections in the early Universe induce $\langle \sigma_{\rm ann} v \rangle_{\rm int}$ to deviate, also sizably, from $\langle \sigma_{\rm ann} v \rangle_0$. This difference in the two cross sections is responsible for the band of values of Υ shown in Fig. 1(a).

When the neutralino relic abundance is low, such that neutralinos are not the dominant component of dark matter, Υ acquires an additional dependence on $\Omega_\chi h^2$ through the rescaling factor ξ^2. This is shown in Fig. 1(b). The effect of ξ^2 is obviously to reduce Υ: the lower the relic abundance, the smaller ξ and thus the flux factor. The lowest points in Fig. 1(b) are the ones with lower values of $\Omega_\chi h^2$. These configurations, even though they give a large $\langle \sigma_{\rm ann} v \rangle_0$ (low $\Omega_\chi h^2$ has large values of $\langle \sigma_{\rm ann} v \rangle_{\rm int}$, and in this case $\langle \sigma_{\rm ann} v \rangle_{\rm int} \propto \langle \sigma_{\rm ann} v \rangle_0$), nevertheless have a low flux factor because they are underabundant. This implies that largely subdominant relic neutralinos are likely to provide (almost) undetectable antiproton fluxes. This is somewhat at variance with the case of direct detection: the difference arises from the fact that the antiproton signal (as well as the other galactic signals) depends quadratically on the dark matter density (and hence on the rescaling factor), while for direct detection the dependence is linear and the suppression is much milder [7].

The situation of MSUGRA is shown in Fig. 2. In this case, the largest values of the flux factor Υ are about an order of magnitude lower that in the EMSSM: $\Upsilon \lesssim 10^{-13}$ GeV^{-4} for light neutralinos. This is a consequence

of the properties of neutralinos in this constrained type of model: neutralinos turn out to be mainly gauginos and their couplings, especially to Higgs bosons, which require a mixed Higgsino-gaugino neutralino content, are in general smaller than in some sectors of the EMSSM. The lower panels in Fig. 2 show the situation in a sector of the MSUGRA scheme where the soft scalar masses are large: $m_0 > 1$ TeV [22,23]. In this sector, the neutralino may acquire a nonvanishing Higgsino component [22,23], as a consequence of the radiative electroweak symmetry breaking, and their couplings to Higgs bosons are enhanced [22]: the consequence on the flux factor is in fact a mild enhancement, up to values of Υ around $(3-4)\times 10^{-13}$ GeV^{-4}, closer to the EMSSM upper values.

D. The differential antiproton spectrum $g(T_{\bar{p}})$

Let us move now to a discussion of differential spectra of antiprotons which are produced by neutralino annihilation. The capability of producing antiprotons depends on the possibility for neutralinos to produce quarks or gluons, either directly or through decay of their annihilation products: quarks and gluons will then hadronize and eventually produce antiprotons. We have modeled the hadronization process by using the PYTHIA Monte Carlo model (MC) [24]. The neutralino annihilation is calculated analytically as described in Ref. [25]. Neutralino annihilation occurs at rest in the galactic frame, and the different final states that are open therefore depend on the neutralino mass. The annihilation may proceed through the following channels: production of a fermion pair; production of WW and ZZ; production of a Higgs boson pair; production of a Higgs boson together with a gauge boson (which can be the Z boson or the W depending whether the Higgs boson is neutral or charged). Apart from the direct production of quarks or gluons, the decay chain of the annihilation products until a quark is produced is calculated analytically. At this stage, the antiproton differential flux is obtained from the MC modeling. More details are given in Appendix A.

A sample of $\bar{p}$ spectra for the four types of neutralino annihilation final states is shown in Fig. 3, for different values of the neutralino mass: panel (a) shows the spectra calculated for annihilation into a pure $b\bar{b}$ state; panel (b) refers to annihilation into a pure ZZ state; panel (c) refers to an annihilation into a Higgs boson pair, where the scalar Higgs boson has a mass of $m_h = 120$ GeV, the pseudoscalar Higgs boson mass is $m_A = 200$ GeV, for $\tan\beta = 10$ and for a vanishing value of the Higgs boson mixing parameter α; panel (d) refers to annihilation into an hZ pair, for $m_h = 120$ GeV, $\tan\beta = 10$, and $\alpha = 0$. Figure 3 shows the dependence of the antiproton spectra on the production energy, fixed by the neutralino mass. For instance, in panel (a) the antiprotons are produced by the hadronization of b quarks injected at the energy given by the neutralino mass; in panel (b), antiprotons are produced by quarks produced by the decay of Z bosons in motion with respect to the neutralino rest frame: a Lorentz boost on the hadronization spectra is therefore operative in shifting the fluxes to larger kinetic energies.

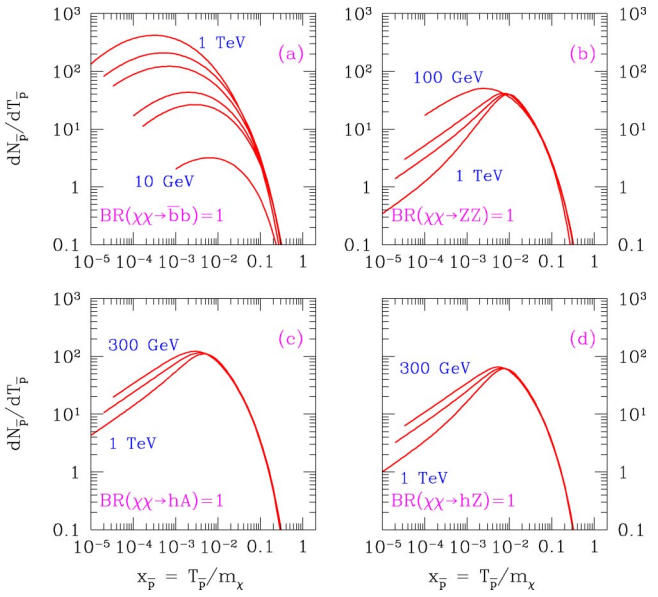

FIG. 3. Antiproton differential energy distribution for pure annihilation channels as a function of the reduced kinetic energy $x_{\bar{p}} \equiv T_{\bar{p}}/m_\chi$. (a) refers to annihilation into a $b\bar{b}$ pair, for neutralino masses of $m_\chi = 10,60,100,300,500,1000$ GeV (from bottom to top); (b) refers to annihilation into a ZZ pair, for $m_\chi = 100,300,500,1000$ GeV (from top to bottom); (c) refers to annihilation into a scalar + pseudoscalar Higgs boson pair hA, for $m_\chi = 300,500,1000$ GeV (from top to bottom), and for $m_h = 120$ GeV, $m_A = 200$ GeV, $\tan\beta = 10$ (ratio of Higgs boson vacuum expectation values) and $\alpha = 0$ (Higgs boson mixing parameter); (d) refers to annihilation into a hZ pair, for $m_\chi = 300,500,1000$ GeV (from top to bottom), and for $m_h = 120$ GeV, $\tan\beta = 10$, and $\alpha = 0$.

Spectra like the ones shown in Fig. 3 are used to calculate the differential spectra $g(T_{\bar{p}})$. However, as it is clear from Eq. (4), we also need to know the values of the branching ratios of each neutralino annihilation final state. The branching ratios will weight the different differential spectra, like the ones shown in Fig. 3. An example of branching ratios for neutralino annihilation is given in Fig. 4 for the EMSSM scheme, and in Fig. 5 for the MSUGRA models.

In the EMSSM, we notice that the annihilation in fermions may be sizable and dominant for masses lower than 500 GeV. The two-Higgs-boson final state is usually of the order of or lower than the $f\bar{f}$ final state, while the gauge boson final state may dominate, except for very large neutralino masses. The mixed gauge+Higgs boson final state tends to be dominant at very large neutralino masses.

In the case of MSUGRA models, since the neutralino tends to be a gaugino which couples effectively to fermions through sfermion exchange, the $f\bar{f}$ final state usually dominates. A relevant production of final states other than fermions, especially gauge bosons, occurs in the large sfermion mass regime ($m_0 > 1$ TeV), where sfermion exchange is suppressed by the large sfermion mass and at the same time a Higgsino component for the neutralino arises: this facilitates the coupling to both Higgs and gauge bosons.

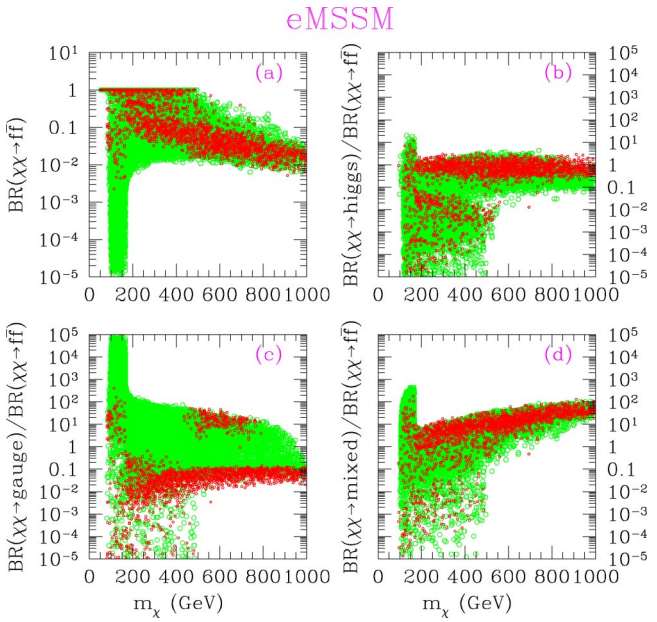

FIG. 4. (Color online) Branching ratios for the neutralino self-annihilation cross section in the EMSSM. (a) shows the amount of the branching ratio for the annihilation into a fermion-antifermion final state ($\chi\chi\rightarrow f\bar{f}$). (b), (c), and (d) show the amount, relative to the $f\bar{f}$ final state, of the annihilation into Higgs bosons, gauge bosons, and the mixed Higgs boson–gauge boson final state. Dark (red) points denote configuration with $0.05\leqslant\Omega_\chi h^2\leqslant 0.3$ (dominant relic neutralinos). Light (green) circles indicate configuration with $\Omega_\chi h^2<0.05$ (subdominant relic neutralinos).

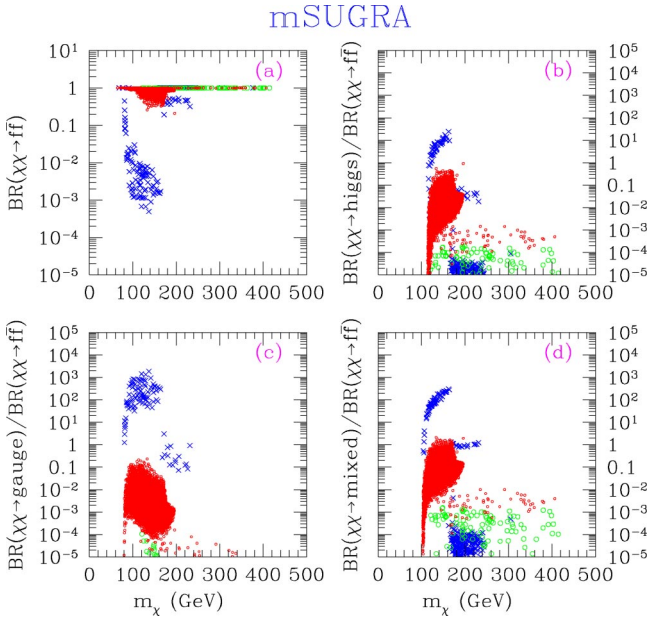

FIG. 5. (Color online) The same as in Fig. 4, calculated in the MSUGRA scheme. Dark (red) points denote configuration with $0.05\leqslant\Omega_\chi h^2\leqslant 0.3$ (dominant relic neutralinos). Light (green) circles indicate configuration with $\Omega_\chi h^2<0.05$ (subdominant relic neutralinos). Crosses (in blue) indicate the MSUGRA configurations with $m_0>1$ TeV.

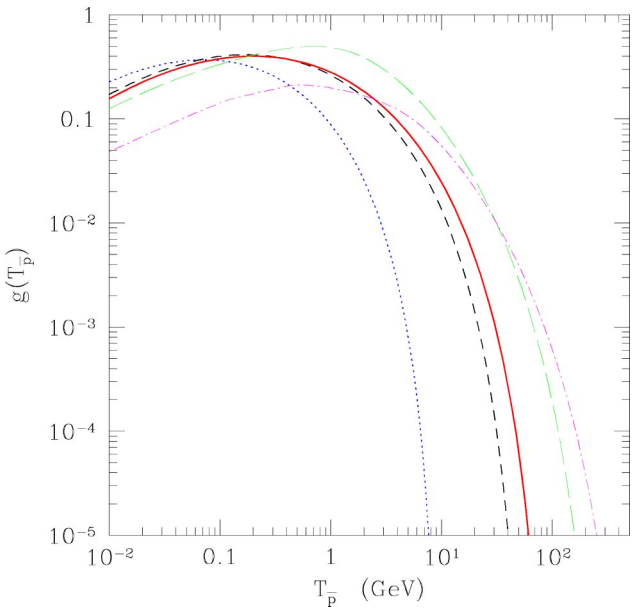

FIG. 6. (Color online) Representative differential antiproton spectra per annihilation event $g(T_{\bar{p}})$ from neutralino self-annihilation, as a function of the antiproton kinetic energy $T_{\bar{p}}$. The different curves refer to different neutralino masses: $m_\chi=10$ [dotted (blue)], 60 [short dashed (black)], 100 [solid (red)], 300 [long dashed (green)], and 500 GeV [dot-dashed (magenta)]. The spectra are selected from our sample of the EMSSM, except the one for $m_\chi=10$ GeV which refers to an EMSSM without grand unification gaugino universality [26,27]. All the spectra refer to neutralinos with $\Omega_\chi h^2=0.1$ and large values of the flux factor Υ. The spectrum for $m_\chi=100$ GeV is the reference spectrum for the analysis of the astrophysical properties in the next sections.

The final result of this analysis is the calculation of realistic antiproton differential spectra for neutralino annihilation. Some representative examples are shown in Fig. 6, for different values of the neutralino mass. All the spectra refer to neutralinos selected to have $\Omega_\chi h^2=0.1$ and large values of the flux factor Υ (close to the upper values of Fig. 1, for each mass). All these spectra properly take into account all the ingredients discussed in this section: the hadronization spectra and the annihilation branching ratios. The spectrum for $m_\chi=100$ GeV is the reference spectrum for the analysis of the astrophysical properties in the next sections. The spectra shown in Fig. 6 are selected from our sample of the EMSSM, except the one for $m_\chi=10$ GeV, which refers to an EMSSM without the grand unification condition between the gaugino mass parameters M_1 and M_2 [26,27]. In this class of models the neutralino can be as light as a few GeV [26,27], in contrast to the standard EMSSM, where LEP constraints imply a lower bound on the neutralino mass of about 50 GeV. For completeness, we have therefore included also the representative spectrum for $m_\chi=10$ GeV, in order to illustrate the effect of propagation on the primary flux from light neutralinos. However, a complete study of the EMSSM without grand unification gaugino universality is beyond the scope of this paper.

Now that we have discussed the source term, we proceed to the second step of the calculation: the study of how these

antiprotons diffuse and propagate in the galaxy and in the solar system. The result of this analysis will be the interstellar and top-of-atmosphere (TOA) fluxes of primary antiprotons.

III. DIFFUSION AND PROPAGATION IN THE GALAXY

The propagation of cosmic rays in the galaxy has been considered in the framework of a two-zone diffusion model, which has been described at length in Refs. [18,19,28]. Here we only recall the main features of this model, and refer to the above-mentioned papers for all the details and motivations. We also present in detail the quantitative dependence of the secondary and primary signals on the propagation parameters.

A. The framework

The disk of the galaxy is described as a thin disk of radius $R=20$ kpc, which contains the interstellar gas with a surface density $\Sigma=2hn_{\rm ISM}$ with $h=100$ pc and $n_{\rm ISM}=1$ cm^{-3}. It is embedded in a thicker diffusion halo, supposed to have a cylindrical shape with the same radius R as the disk and height L which is not well known. The matter density is much lower in the diffusion halo so that spallations (rate $\Gamma \equiv 2hn_{\rm ISM}\sigma$ yielding the secondary species) of the charged nuclei occur only in the disk. Moreover, the standard sources also happen to be located in the disk.

The spatial diffusion of cosmic rays is assumed to occur uniformly in the whole (disk and halo) diffusion volume, with the same strength. The corresponding diffusion coefficient has been defined as $K(E)=K_0\beta(\mathcal{R}/1\ {\rm GV})^{\delta}$, where $\mathcal{R}$ stands for the particle rigidity and K_0 and δ are free parameters of the model. We also consider the possibility that a galactic wind blows the particles away from the disk in the z vertical direction, with a constant speed V_c. It induces an adiabatic dilution of the energy of the particles in the disk due to the sudden change in V_c. Several other processes modify the antiproton energy distribution: ionization losses when interacting with the neutral interstellar matter, or from Coulomb losses in a completely ionized plasma, dominated by scattering off the thermal electrons. To end with, minimal reacceleration on random hydrodynamic waves, i.e., diffusion in momentum space, described by a coefficient K_{pp} related to the spatial diffusion $K(E)$, is inevitable [29]. This process is assumed to occur only in the disk and is related to the velocity of disturbances in the hydrodynamical plasma V_A, called the Alfvén velocity. In summary, our diffusion model has five free parameters K_0,δ,L,V_c,V_A which describe the minimal number of physical effects thought to have some role in antiproton propagation.

The sets of diffusion parameters were constrained in a previous work [19] (see also Ref. [30]) by analyzing stable nuclei (mainly by fitting the boron to carbon ratio B/C). The values we obtained were also shown to be compatible with the observed secondary antiprotons [18] and the flux of radioactive isotopes [31]. However, in a first step we will disregard these constraints: in order to clarify which of the propagation parameters are important if one wants to compare any possible primary component to the background (secondaries), we study the effect of each parameter on the signal and the background. Only in a second step is this additional information on the constraints used to draw conclusions about the variation that will result in the primary supersymmetric signal (see Sec. IV A).

B. Solutions for primary and secondary antiprotons

We are interested in the cosmic ray antiproton flux

$$\Phi^{\bar{p}}(r,z,E)=\frac{v_{\bar{p}}}{4\pi}N^{\bar{p}}(r,z,E). \tag{8}$$

It is related to the differential density $N^{\bar{p}}(r,z,E) \equiv dN^{\bar{p}}(r,z,E)/dE$ which satisfies the steady-state diffusion equation. The general procedure for solving this equation as well as references for a detailed derivation are given in Appendix B. At variance with the solutions already presented elsewhere, it proves to be useful, as suggested by a study of the spatial origin of secondary and primary cosmic rays CRs (see Ref. [32] for what is ment by ''spatial origin''), to introduce the quantities

$$r_{\rm w}\equiv\frac{2K(E)}{V_c}, \tag{9}$$

$$r_{\rm sp}\equiv\frac{K(E)}{h\Gamma_{\rm inel}(E)}. \tag{10}$$

Since many configurations of $K(E)=K_0\beta\mathcal{R}^{\delta}$ and V_c lead to the same $r_{\rm w}$ and $r_{\rm sp}$, these new parameters automatically avoid a useless discussion about many degenerate values of the diffusion coefficient and make the dependence on the important parameters more evident in formulas (the physical meaning of these new parameters is explained below; see also Ref. [32]).

The solutions are given below discarding energy redistributions (see Appendix for the procedure to include them). Energetics are not the dominant effects so it is interesting to focus on the analytical formulas obtained in that case.

(*a*) *The primaries*. Let us first inspect the primaries: the source term is given by $q_{\bar{p}}^{\rm SUSY}(r,z,T_{\bar{p}})$ described by Eq. (1) and discussed in detail in Sec. II. Primary antiprotons are produced throughout the whole diffusive halo, which is embedded in the dark matter halo. An advantage when energy losses and gains are discarded is that the solution can be recast as (see Appendix B)

$$N^{\bar{p},{\rm prim}}(r=R_{\odot},z=0,E)=\mathcal{E}^{\rm prim}_{\rm source}(E)\times S^{\rm prim}_{\rm astro}(R_{\odot},0,E),$$

where the *elementary* source term (spectrum from a point source) given by

$$\mathcal{E}^{\rm prim}_{\rm source}(E)\equiv\Upsilon g(T_{\bar{p}}) \tag{11}$$

can be separated from the astrophysical part

$$S^{\rm prim}_{\rm astro}(R_\odot,0,E)\equiv\sum_{i=1}^{\infty}\Pi_i(E,R_\odot)\left\{\int_0^R J_0(\zeta_i r/R)\times\int_{-L}^{L}e^{-z/r_{\rm w}}\frac{\sinh[S_i(L-z)/2]}{\sinh[S_iL/2]}\times w(r,z)\right\}dzrdr. \quad (12)$$

In the above equation, $w(r,z)$ is the *effective* spatial distribution of the primary sources [e.g., $\rho^2_{\rm DM}(r,z)$ for supersymmetric particles and $\rho_{\rm DM}(r,z)$ for evaporating primordial black holes (PBHs)]. We have defined

$$\Pi_i(E)\equiv\frac{2}{\bar{A}^p_i(E)R^2J_1^2(\zeta_i)}\times J_0(\zeta_i R_\odot/R). \quad (13)$$

We also use

$$\bar{A}^p_i(E)=K(E)\left\{2r_{\rm sp}^{-1}(E)+2r_{\rm w}^{-1}(E)+S_i\coth\left(\frac{S_iL}{2}\right)\right\} \quad (14)$$

and

$$S_i=\sqrt{4r_{\rm w}^{-2}(E)+4\zeta_i^2/R^2}. \quad (15)$$

The functions J_0 and J_1 are, respectively, the Bessel functions of zeroth and first order, and ζ_i is the ith zero of J_0. The superscript $\bar{p}$ in $\bar{A}^p_i(E)$ indicates that the term $r_{\rm sp}$ should be evaluated for the antiproton destruction rate and at the parent rigidity.

Compared to Eq. (1), which describes the supersymmetric source term at each position (r,z), we isolated in the new term $\mathcal{E}^{\rm prim}_{\rm source}(E)$ the only required information about the production process. For antiprotons produced by neutralino annihilations, the flux factor Υ (see Sec. II C) and the *elementary* spectrum $g(T_{\bar{p}})$ (see Sec. II D) are fully described by the properties of the supersymmetric and hadronization models. As a result, $S^{\rm prim}_{\rm astro}(R_\odot,0,E)$ is solely dependent on the propagation properties and the effective spatial source distribution $w(r,z)$. This function is all we need in order to discuss the propagation uncertainties on the primary fluxes, i.e., the signal detected at solar location $R_\odot$.

(*b*) *The secondaries.* The secondaries are produced from proton sources distributed according to the spatial supernova remnant distribution in the thin disk $2h\delta(z)q(r)$. These protons are first propagated, leading to an equilibrium distribution $N^p(r,z,E)$, which in turn produces secondary antiprotons when it interacts with the interstellar gas. Compared to primaries, secondaries diffuse twice. Actually, it is not possible, strictly speaking, to isolate an elementary source term as for primaries (we skip the details, but the interested reader can inspect the structure of the equations in Ref. [18]). However, it is possible to overcome this shortcoming. Antiprotons are produced only by protons that are beyond the threshold of 7 GeV; in the term A^p_i that originally appears in the secondary solution (see, e.g., Ref. [18]), and that prevents this separation, one can neglect spallations and convection (high-energy regime) and approximate

$$A^p_i\approx K(E)\times 2(\zeta_i/R)\coth(\zeta_i L/R).$$

It is then possible to recast the various terms entering the solution in order to obtain a formula that (as for primaries) isolates the dependence on the propagation terms:

$$\bar{N}^{p,\rm sec}(r=R_\odot,0,E)\approx\mathcal{E}^{\rm sec}_{\rm source}(E)\times B^{\rm sec}_{\rm astro}(R_\odot,0,E). \quad (16)$$

The corresponding terms are

$$\mathcal{E}^{\rm sec}_{\rm source}(E_{\bar{p}})\equiv\int_{E_{\rm thresh}}^{\infty}\frac{Q(E_p)}{K(E_p)}\frac{d\sigma(E_p,E_{\bar{p}})}{dE_p}dE_p \quad (17)$$

and

$$B^{\rm sec}_{\rm astro}(R_\odot,0,E)\equiv\sum_{i=1}^{\infty}\frac{\Pi_i(E,R_\odot)}{2(\zeta_i/R)\coth(\zeta_i L/R)}\times\left\{\int_0^R J_0(\zeta_i r/R)2hq^{\rm disk}(r)\right\}rdr. \quad (18)$$

This approximate solution is used only to estimate the sensitivity of the fluxes to the diffusion parameters. We go back to the full solution (see Ref. [18] and Appendix B for more references) when the final results are presented.

(*c*) *Sensitivity to the propagation parameters.* With the quantities defined above, it is straightforward to evaluate primary and secondary fluxes "as if" the elementary production processes were the same (to focus on the astrophysical uncertainties). This defines the relative sensitivity to the propagation parameters, and it is merely the ratio of the *astrophysical* part of the signal S to the background B:

$$\mathcal{S}[\rm Par]\equiv\frac{S^{\rm prim}_{\rm astro}(R_\odot,0,E)}{B^{\rm sec}_{\rm astro}(R_\odot,0,E)}. \quad (19)$$

This ratio is likely to depend on the propagation parameters, in the first place because primary sources are located in the whole diffusive halo, whereas secondary sources are induced spallatively in the thin disk only.

We now investigate how the primary flux $S^{\rm prim}_{\rm astro}$, secondary flux $B^{\rm sec}_{\rm astro}$, and relative sensitivity $\mathcal{S}$ depend on the propagation parameters $K(E)$, $r_{\rm w}$, $r_{\rm sp}$, L, R, and $R_\odot$ and on the effective source distribution $w(r,z)$. This discussion will be general and apply to any primary species. It is discussed below for the case of supersymmetric primaries, but we will also plot (but not comment on) the results for PBH antiprotons.

C. Evolution of fluxes with astrophysical parameters

We now review each one of the above parameters, starting with the diffusion coefficient $K(E)=K_0\beta\mathcal{R}^{\delta}$. This parameter induces a change in both the normalization—through K_0 and only in the high-energy regime—and the energy depen-

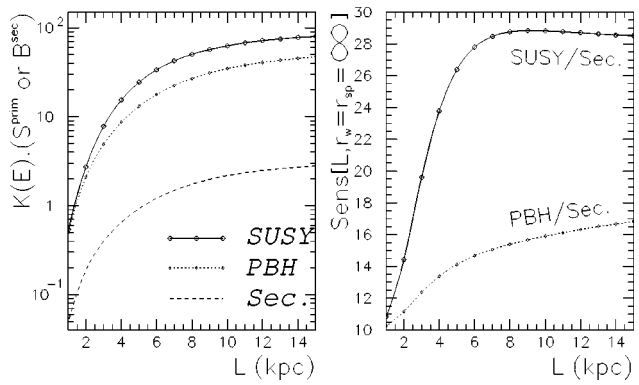

FIG. 7. This plot displays the quantities $K(E)\times S^{\rm prim}_{\rm astro}$ and $K(E)\times B^{\rm sec}_{\rm astro}$, see Eqs. (12) and (18) (left panel) and $\mathcal{S}$ defined by Eq. (19) (right panel), as a function of the propagation parameter L ($r_{\rm w}=r_{\rm sp}=\infty$, i.e., no wind, no spallations) for an isothermal profile. Two cases have been considered for the primary signal. The curve labeled "supersymmetric" corresponds to an effective source term proportional to $w(r,z)=\rho^2_{\rm DM}$, whereas the curve PBH corresponds to a source term proportional to $w(r,z)=\rho_{\rm DM}$, as for primordial black holes.

dence (through $\mathcal{R}^{\delta}$). At sufficiently high energy (above a few tens of GeV), $r_{\rm w}, r_{\rm sp} \gg 1$ and A_i and S_i become independent of E, so that the sole energy dependence $1/K(E)$ is factored out of $\Pi_i(E,R_\odot)$, i.e., of the Bessel sums. As a result, the quantity $\mathcal{S}$ is insensitive to the choice of $K(E)$, whatever the value of the other parameters. There is one subtlety left: the secondary *elementary* production $\mathcal{E}^{\rm sec}_{\rm source}(E)$, as defined above, in contrast to that of the primary, is not fully elementary, because it does depend on the value of $K(E_p)$ above 7 GeV. However, as we will see later, all propagation parameters are designed to have about the same $K(E)$ at 100 GeV, so that the quantity $N^{p,\,\rm prim}/N^{p,\,\rm sec}(r=R_\odot,0,E)$ is eventually not very sensitive to this parameter.

1. The diffusive halo size L and the radius R of the galaxy

These parameters are related to the escape probability from the confinement volume (the magnetic halo of the galaxy). The larger L and R, the greater the probability for particles emitted in remote sources to reach us. Actually, the side boundary plays almost no role for several reasons. First, escape is driven by the closest boundary, which is the one at $z=\pm L$ as L is likely to be smaller than R; second, the source distribution is peaked near the galactic center and decreases to very small values at large radii (see Ref. [32] for more details). Hence, for $L \lesssim 5$ kpc, setting $R=20$ kpc or $R=\infty$ leaves S and B unchanged. The enhancement of fluxes with L can be seen in Fig. 7 (we use here and in other figures the isothermal profile for the dark matter distribution), showing $\mathcal{S}[L,r_{\rm w}=\infty,r_{\rm sp}=\infty]$ as a function of L (we limit the discussion to the supersymmetric case, but the reader can straightforwardly extend to PBH's). For small L, only the sources very close to the solar neighborhood contribute and, as the dark matter source distribution is normalized to 1, the supersymmetric and PBH cases yield the same value. As L increases, escape is less efficient, and more sources (secondary or primary) effectively contribute to the signal. This enhancement is more important for primaries than for secondaries, as the effective number of sources increases, respectively, as L^3 (volume distribution) and L^2 (surface distribution). In the case of primaries, part of the enhancement is also due to the mere fact that the number of sources within the diffusive box increases with L (we recall that the sources from the dark halo to be propagated are those enclosed inside the diffusive box; see Ref. [14]). Both effects are responsible for the evolution of $\mathcal{S}$. For $L \gtrsim 5$ kpc, no further significant enhancement is observed, as the bulk of the primary sources (the core radius of the dark matter distribution) is then almost entirely enclosed in the diffusive halo. To be quantitative, $\mathcal{S}$ is increased by a factor of 3 for $L=15$ kpc compared to $L=1$ kpc. Notice that the quantity $K(E)\times S^{\rm prim}_{\rm astro}$ plotted in the left panel of Figs. 7, 8 and 9 does not depend on $K(E)$. To understand this property it is sufficient to look at the expression for $S^{\rm prim}_{\rm astro}$ in Eq. (12).

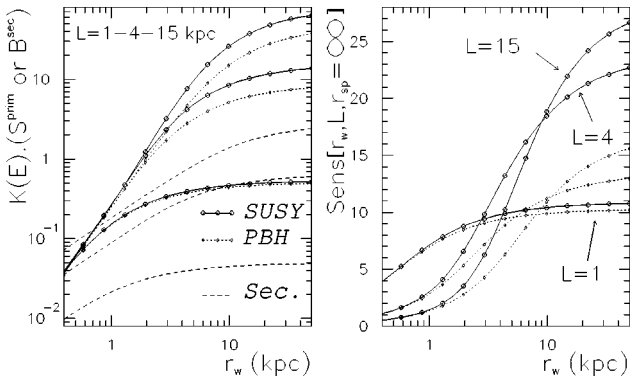

FIG. 8. Same quantities as in Fig. 7, but as a function of the propagation parameter $r_{\rm wind}$, and for three values of L ($r_{\rm sp}=\infty$).

2. The galactic wind V_c through r_w

At high energy (generally a few tens of GeV), propagation is dominated by diffusion. At low energy convection may become the most efficient process (parameter $r_{\rm w} \approx 1$; see Refs. [32,33]) and it may compete with L for escape. The effect of convection is to blow the particles away from the disk, leading to an effective size of the diffusive halo $L^\star \sim r_{\rm w}$. There is a difference from the effect of L as the de-

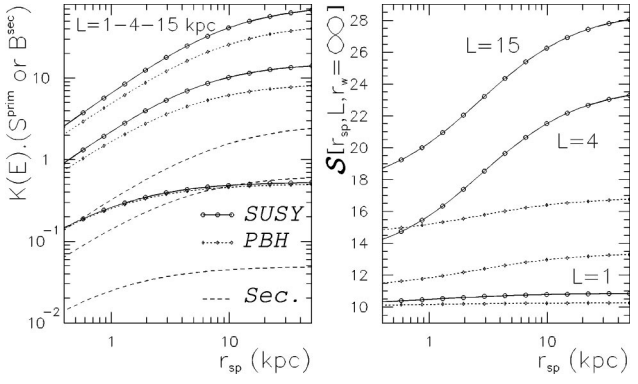

FIG. 9. Same quantities as in Fig. 7, but as a function of the propagation parameter $r_{\rm sp}$, and for three values of L ($r_{\rm w}=\infty$).

crease of r_w does not lead to a decrease of the number of primary sources enclosed in the diffusive volume. However, it turns out that the effect of the galactic wind is also more important for primaries than for secondaries, as the flux is exponentially decreased with z for particles created at height z in the diffusive halo. This can be seen in Fig. 8 (left panel). We clearly see the competition between L and r_w in the right panel. For large L, the evolution of $\mathcal{S}$ is completely driven by r_w, so that we can compare the result to those of Fig. 7. When wind is present, the sensitivity to a signal is much more reduced than that we would obtain with a similar L (i.e., a factor ~ 25 in $\mathcal{S}$ between the cases $r_w = 1$ kpc and $r_w = 15$ kpc, compared to a factor of 3 for L in the same range). For small r_w, all primary curves converge to the same value, independently of L, because then the cosmic rays become blind to this boundary, being convected away before having a chance to reach the top or bottom of the box.

3. The relative rate of spallation through r_{sp}

At low energy, particles can be destroyed more easily, because the probability of crossing the disk, and thus interacting with matter, increases relative to the escape (diffusive or convective) probability. The dependence of $\mathcal{S}$ on r_{sp} is displayed in Fig. 9.

When r_{spal} increases, we are sensitive to sources located farther away, and as for L and r_{wind}, the effect is more important for primaries than for secondaries. However, the effect of r_{spal} is milder. This is because the cutoff due to spallations is less efficient than escape or convective wind in preventing particles coming from faraway sources from reaching us.

D. A comment about secondaries from GALPROP model

Among several other models that are used to describe cosmic-ray propagation, the fully numerical approach implemented in GALPROP [34] has been widely used. Some results obtained within this framework, in particular when studying the secondary antiproton spectrum, seem to differ (see, e.g., Ref. [35]) from ours, obtained with a semianalytical model. In our paper we want to derive constraints on the supersymmetric contribution which can be added to the secondary one, when confronting with data. Therefore, we take the opportunity of this specific work to briefly summarize and discuss some of the differences between the two approaches and their results.

First, the approximation that may appear crucial is that, in order to find analytical expressions for the cosmic ray density, we have to use a simplified description of the matter distribution in the galaxy, whereas with a numerical approach any distribution can be considered. However, the results are not strongly affected by this hypothesis. In the framework of steady-state diffusion models, [32] has shown that the stable nuclei detected in the solar neighborhood were emitted from sources located in a region large enough so that, having sampled very different regions of the galactic disk, they are sensitive to a mean density. Moreover, introducing a radial dependence of the matter distribution does not induce sizable difference in the results [36]. In relation to this first point, we have to emphasize that Ref. [35] actually does not use a detailed description of the local (i.e., on a scale of a few hundreds of pc) gas distribution. As a result, the authors cannot provide a reliable analysis of the radioactive species, which are very sensitive to the local structure of the interstellar medium [31].

Second, the numerical approach is still costly in terms of computation time, and is less suited to the systematic study of different effects. For example, Ref. [34] using a predefined small value $\delta = 0.3$ for the diffusion coefficient spectral index, finds that the observed spectrum of B/C requires small values of the galactic wind. Indeed, a full scan of the parameter space, extended to a range of values for δ, revealed that models with higher values of δ and with larger values of the galactic wind, were actually preferred. This and other results have been thoroughly discussed in Ref. [30], and also compared with different propagation models (such as GALPROP). This point is of great importance for the present work, as the theoretical uncertainties in the antiproton flux are underestimated if some parameters are not varied over all their plausible values.

The last relevant difference is actually not related to the astrophysical model but to the production cross sections. In particular, those relevant for B/C have been recently updated (see references in Ref. [35]), whereas we use a standard set (see, references, e.g., in Ref. [19]). This is a possible way to explain the discrepancy between the secondary antiproton flux, but we estimate that this is unlikely. Indeed, the two sets of cross sections differ mainly at low energy, for which the weight of experimental data is not the greatest. Using the updated set should not change the propagation parameters derived from B/C and used to propagate antiprotons; the final results would essentially remain unaffected.

To conclude, we do not see any physically relevant difference between the two approaches, and they are probably equally valuable. There is still some work to be done from both sides to understand the origin of the differences in the results, which may lie in the methods and interpretation of the results, more than in the models themselves.

IV. RESULTS AND UNCERTAINTIES FOR THE PRIMARY FLUXES

We now use all the ingredients previously discussed (as well as all energy changes) to evaluate the primary interstellar flux. We try to quantify all the uncertainties that could hamper a clear selection or exclusion of supersymmetric configurations. They are substantially induced by the degeneracy in propagation parameters (see Sec. IV A) [19,30] and the choice of a peculiar dark matter profile (see Sec. IV B).

A. Primary fluxes and related uncertainties

The propagation parameters have been constrained by an analysis of the observed boron to carbon (B/C) ratio, by means of a $\chi^2_{B/C}$ test over 26 data points and five free parameters [19]. The best $\chi^2_{B/C}$ was found to be 25.5. A value of 40 was considered quite conservative, corresponding roughly to

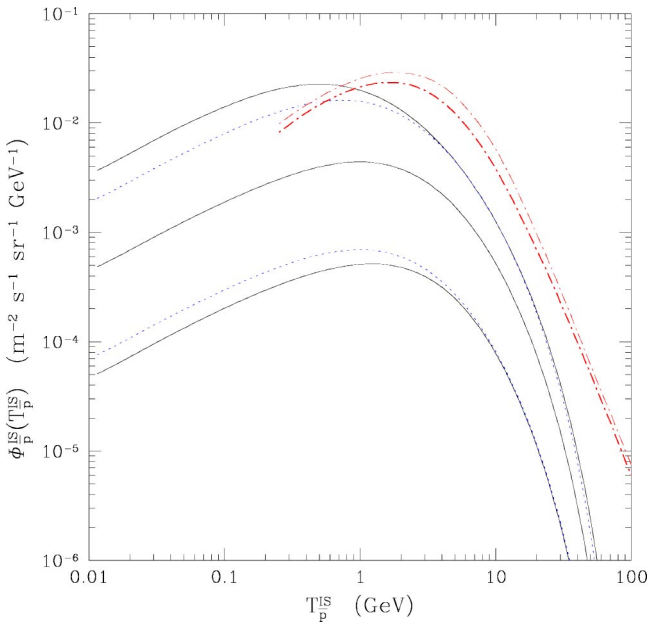

FIG. 10. The solid lines represent the antiproton flux for an $m_\chi = 100$ GeV neutralino and for maximal, median, and minimal astrophysical configurations, for $\chi^2_{B/C} \leq 40$. Dotted lines: the same, but for $\chi^2_{B/C} \leq 30$. The dot-dashed band corresponds to the secondary flux as taken from Ref. [19] for all the configurations giving $\chi^2_{B/C} \leq 40$.

the 4σ confidence level on B/C data interpretation, while a $\chi^2_{B/C} = 30$ can be assigned to about the 2σ confidence level [19].

In Fig. 10 we present the result for the primary antiproton flux for our reference source term for $m_\chi = 100$ GeV, whose $g(E)$ is plotted in Fig. 6. We plot the fluxes corresponding to the parameters providing the maximal and minimal fluxes when all the astrophysical configurations are taken to be compatible with the analysis on stable nuclei, i.e., $\chi^2_{B/C} < 40$. For the same set of astrophysical parameters we also plot the secondary antiproton flux. The variation of the astrophysical parameters induces a much larger uncertainty on the primary than on the secondary flux: in the first case, the uncertainty reaches two orders of magnitude for energies $T_{\bar{p}} \lesssim 1$ GeV, while in the second case it never exceeds 25% (notice that these uncertainties are smaller than the nuclear ones; see Ref. [18]). A thorough discussion about why a combination of parameters gives the same secondary flux is skipped here, but the reader is referred to Ref. [30] for more details. The large variation in the primary signal can be understood from the previous discussion: first, the exotic signal is more sensitive to astrophysical parameters than the standard, as already underlined. Second, this has to be weighted by the fact that the secondary flux has in its source term an additional $K(E)$. While many combinations of K_0, δ, L, and V_c lead to the same secondary flux, it is not straightforward to decipher which ones lead to the maximum and minimum primary fluxes. Decreasing L and r_w decreases the flux, but at the same time, to keep the fit to B/C good, K_0 has to be decreased also [19,30], in turn increasing the flux [primaries depend on $1/K(E)$]. However, the first two parameters are more important (especially the wind effect) than the latter. We give in Table I the values for these parameters yielding the maximum and minimum of the error band in both primary and secondary fluxes. The resulting variation in Fig. 10 can be read off from Figs. 7, 8, and 9 (left panels) and Table I: a factor ~ 2000 because of r_w and L, an additional factor $\lesssim 4$ for r_{sp} (see Fig. 9, left panel) divided by a factor ~ 50 because of the value of $K(E)$, leading to a net scattering of ~ 100. This is almost independent of the specific supersymmetric configuration.

As emphasized before, energy redistributions relate a specific supersymmetric configuration [by means of $g(T_{\bar{p}})$] to the given propagation configuration. The effect on the resulting antiproton flux is expected to be mild. We show in Fig. 11 the result of our analysis for the representative EMSSM spectra shown in Fig. 6, corresponding to $m_\chi = 60,100,300,500$ GeV and for the median astrophysical parameters. The low-energy behavior of the fluxes is similar for all the masses: this is a consequence of the propagation of the source spectra, which reduces the intrinsic differences in the original fluxes at low kinetic energies. The high-energy behavior of the fluxes reflects the fact that for higher neutralino masses the phase space for antiproton production is larger. Since neutralinos in the galaxy are highly nonrelativistic, their mass acts as an effective cutoff on the antiproton production kinetic energy.

The effect of propagation on the primary antiproton spectrum may also be shown by the following function [13]:

$$C^{prop}_{SUSY}(T_{\bar{p}}) = \frac{\Phi_{\bar{p}}(R_\odot, 0, T_{\bar{p}})}{\Upsilon g(T_{\bar{p}})}, \tag{20}$$

where $\Phi_{\bar{p}}(\odot, T_{\bar{p}})$ is the interstellar antiproton flux after propagation, normalized to supersymmetric elementary production term. The propagation function $C^{prop}_{SUSY}(T_{\bar{p}})$ is a measure of how the source fluxes are deformed by propagation

TABLE I. Astrophysical parameters giving the maximal, median, and minimal supersymmetric antiproton flux and compatible with B/C analysis ($\chi^2_{B/C} < 40$). r_w and r_{sp} (kpc) are also given for two kinetic energies 1 GeV and 10 GeV.

Case	δ	K_0 (kpc^2/Myr)	L (kpc)	V_c (km/s)	V_A (km/s)	$\chi^2_{B/C}$	r_w (kpc) [1 GeV/10 GeV]	r_{sp} (kpc) [1 GeV/10 GeV]
max	0.46	0.0765	15	5	117.6	39.98	29.0/73.0	26.0/57.0
med	0.70	0.0112	4	12	52.9	25.68	2.4/9.2	4.4/15.0
min	0.85	0.0016	1	13.5	22.4	39.02	0.33/1.8	0.69/3.1

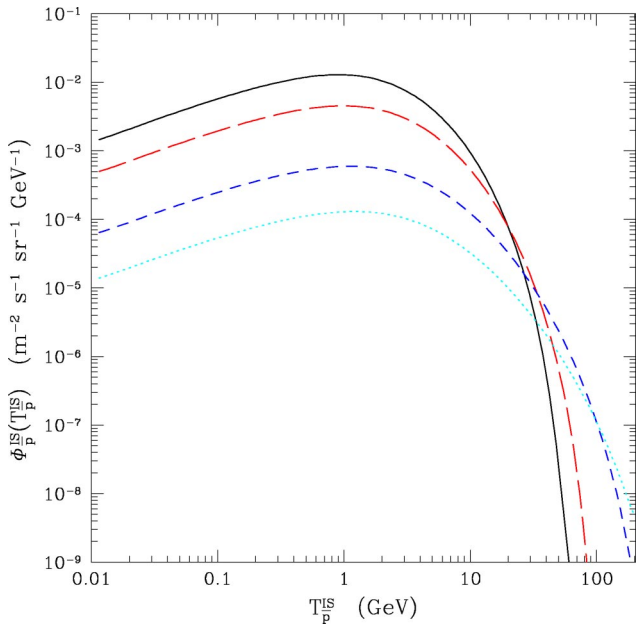

FIG. 11. Interstellar primary fluxes calculated as a function of the antiproton kinetic energy. The fluxes are calculated for the median set of astrophysical parameters. Solid, long dashed, short dashed, and dotted lines correspond to $m_\chi = 60,100,300,500$ GeV, respectively. The fluxes correspond to the representative differential antiproton spectra shown in Fig. 6.

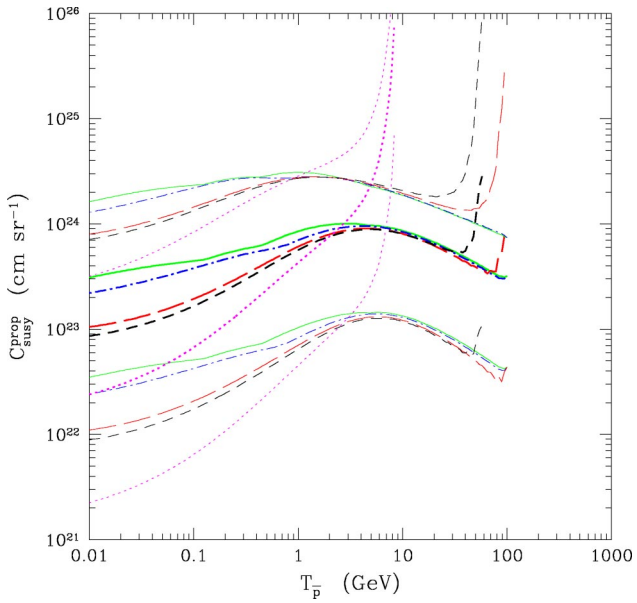

FIG. 12. Propagation function $C_{\rm SUSY}^{\rm prop}$ of the primary supersymmetric antiproton fluxes as a function of the antiproton kinetic energy, calculated for the reference fluxes of Figs. 6 and 11. Dotted lines refer to $m_\chi = 10$ GeV, short dashed to $m_\chi = 60$ GeV, long dashed to $m_\chi = 100$ GeV, dot dashed to $m_\chi = 300$ GeV, and solid to $m_\chi = 500$ GeV. For each set of curves, the upper, medium, and lower lines refer to the maximal, median, and minimal sets of astrophysical parameters.

and diffusion before reaching the solar position in the galaxy and is shown in Fig. 12 for the same representative spectra of Fig. 6. The energy dependence is steeper for low-mass neutralinos, and it becomes somewhat more symmetric around the maximal values for neutralinos of increasing mass. The steep rise of $C_{\rm SUSY}^{\rm prop}(T_{\bar{p}})$ near the end of the antiproton production phase space at $T_{\bar{p}} = m_\chi$ is due to reacceleration: while the source factor $g(T_{\bar{p}})$ is rapidly vanishing, the propagated flux $\Phi_{\bar{p}}(R_\odot,0,T_{\bar{p}})$ decreases in a much milder way because of reacceleration effects. This effect is more pronounced for the maximal astrophysical configuration, where V_A is maximal, and it disappears if V_A is set to zero. Figure 12 also shows that the maximal, median, and minimal sets of astrophysical parameters affect not only the absolute magnitude of the fluxes but also their energy dependence: the distortion of the original flux differs depending on the values of the propagation parameters, as discussed in the previous sections. In particular, the energy of maximal transfer for neutralino masses above 60 GeV shifts from about 1–2 GeV for the maximal set to 5–6 GeV for the minimal set. Figure 12 shows, at low kinetic energies, a hierarchy in the behavior of $C_{\rm SUSY}^{\rm prop}(T_{\bar{p}})$ which follows the hierarchy of the neutralino masses: the propagation function is larger at low energies for heavier neutralinos, i.e., for harder antiproton fluxes.

The propagation function $C_{\rm SUSY}^{\rm prop}(T_{\bar{p}})$ can be used directly to estimate the propagation effects once the supersymmetric production term $\Upsilon g(T_{\bar{p}})$ is known.

B. Uncertainties related to the dark matter distribution

We have performed all the calculations assuming that the galactic dark matter is distributed as an isothermal sphere with a core radius $a = 3.5$ kpc and local dark matter density $\rho_l = 0.3$ GeV cm^{-3}. For this density profile, we estimated that the antiproton propagation induces an uncertainty on the primary antiproton flux of about two orders of magnitude, especially at low kinetic energies.

Another source of uncertainty on the primary flux comes from the shape of the dark matter density profile, which is only poorly known, and from the allowed range of values of ρ_l for any given density distribution. We have already commented that for an isothermal spherical distribution the local dark matter density may range from 0.18 GeV cm^{-3} to 0.71 GeV cm^{-3}. Moreover, the dark matter distribution may be quite different from a simple isothermal sphere (see, for instance, Refs. [21,37–40] and references therein): the cold dark matter distribution could be nonspherically symmetric, it can be singular at the galactic center, as suggested from numerical simulations, or it can present a clumpy distribution in addition to a smooth component. Since the shape of the galactic halo enters as $\rho_{\rm DM}^2(r,z)$ in the evaluation of the astrophysical part for the primary signal $S_{\rm astro}^{\rm prim}(R_\odot,0,E)$, it is a main ingredient in the determination of the primary antiproton flux, and the uncertainties in the description of $\rho_{\rm DM}(r,z)$ may sizably affect the predicted signal.

The uncertainty in ρ_l, determined by a detailed modeling of the galactic component [39,40] and mainly due to the value of the local rotational velocity [21], depends on the shape of the galactic halo. For the same isothermal sphere, the range in ρ_l may change the primary fluxes by a factor that ranges from 0.36 to 5.6: overall, even for the simple choice of an isothermal sphere, the antiproton flux has an

TABLE II. Sensitivity to the core radius of an isothermal profile, and comparison of the Navarro-Frenk-White (NFW) and isothermal profiles, for three representative propagation sets at $T_{\bar{p}}=1$ GeV. These propagation parameters correspond to the minimum, median, and maximum primary fluxes compatible with nuclei analysis. The reference value $S_{\rm ref}^{\rm prim}$ is for an isothermal halo whose core radius is $a=3.5$ kpc. Notice that for higher energies the results would be the same as those provided by the set $L=15$ kpc (purely diffusive transport).

L(kpc), $r_{\rm w}$, $r_{\rm sp}$	$\frac{S_{a=2.5}^{\rm prim}-S_{\rm ref}^{\rm prim}}{S_{\rm ref}^{\rm prim}}$	$\frac{S_{a=5}^{\rm prim}-S_{\rm ref}^{\rm prim}}{S_{\rm ref}^{\rm prim}}$	$\frac{S_{\rm NFW}^{\rm prim}-S_{\rm ref}^{\rm prim}}{S_{\rm ref}^{\rm prim}}$
15, 28.66, 25.54	-69.5%	$+23.9\%$	$+19\%$
4, 2.38, 4.41	-21.5%	$+9.9\%$	$\sim 0\%$
1, 0.33, 0.69	$<1\%$	$<0.2\%$	$\sim 0\%$

uncertainty of a factor of about 15, on top of the two orders of magnitude due to antiproton propagation. We anticipate that, among all the uncertainties due to the shape of the galactic halo, the uncertainty coming from ρ_l will turn out to be the most relevant one (apart from, eventually, the presence of close clumps).

Independently of the normalization ρ_l, any given density profile could, in principle, modify the signal. In particular, distribution functions derived from numerical simulations are singular toward the galactic center, where a very high neutralino annihilation rate would then occur. We could thus expect that such dark matter profiles would induce an enhanced antiproton flux with respect to a nonsingular distribution. In this class of modified density profiles we can also include an isothermal sphere with different values of the core radius a. We expect that enlarging the core radius would increase the signal. We therefore estimated the modification of the cosmic antiproton flux when different core radii and dark matter profiles are used in the source term. The reference flux is obtained with our spherical isothermal distribution, with core radius $a=3.5$ kpc. The results are shown in Table II. Notice that we have used for all the profiles the normalization $\rho_l=0.3$ GeV cm^{-3}, in order to extract the change of the antiproton flux which is due entirely to the different shapes of the halos. It is clear that each density profile will have to be further implemented with its own value of ρ_l [21,39,40]. From Table II we notice, first of all, that for small L and $r_{\rm w}$ we are completely blind to what occurs near the galactic center. Only the very local properties of the dark matter distribution are of some relevance for our study. For a diffusive halo of 4 kpc, we varied the core radius of the isothermal distribution from 2.5 to 5 kpc. With respect to our reference values of 3.5 kpc, small a leads to a reduction of the flux by about 20%, while large values of a give a 10% increase. For $L=15$ kpc—and all the other propagation parameters modified consequently—a 2.5 kpc core radius diminishes the reference flux by 70% and a 5 kpc one pushes it up by 25%. The uncertainty of a factor of 2 on the core radius of the isothermal distribution then reflects in a factor of 4 indeterminacy of the primary antiproton flux. As for the singular density profiles, Table II shows that a NFW [38] distribution function does not strongly modify the flux: when compared to the isothermal case, the flux is increased by no more than about 20%, and this occurs when the diffusive halo size is the largest. For $L\lesssim 5$ kpc, the difference between an isothermal profile and a NFW singular distribution is irrelevant. This result clearly shows that it is very improbable for an antiproton produced at the galactic center to reach the Earth.

Finally, one can deal with halos which contain regions of enhanced density called clumps. In these subhalos, the neutralino annihilation is more effective and the signal can be increased by some enhancement factor. However, as also suggested by Ref. [41], this enhancement is not propagation dependent and simply acts on the antiproton flux as a normalization factor. From the analysis of Ref. [41], the average enhancement is likely to be smaller than a factor of 5. A detailed analysis of this point is beyond the scope of our paper; however, the effects of such an enhancement are briefly discussed at the end of Sec. V.

In conclusion, we wish to remark that our choice of an isothermal sphere with a core radius $a=3.5$ kpc and local dark matter density $\rho_l=0.3$ GeV cm^{-3}, together with the best choice for the astrophysical parameters which govern diffusion and propagation in the galaxy, represent an optimal choice for the prediction of the antiproton signal. Our results will not be dramatically modified by a different choice for the density profile, while a different choice for the local dark matter density is easily taken into account as a normalization factor.

V. TOP-OF-ATMOSPHERE FLUXES: COMPARISON WITH DATA AND RESULTS FOR SUPERSYMMETRIC MODELS

Now that we have calculated the interstellar fluxes of antiprotons at the Sun's position in the galaxy, we have to further propagate them inside the heliosphere, where the cosmic-ray particles which eventually reach the Earth are affected by the presence of the solar wind. We model the effect of solar modulation by adopting the force field approximation of the full transport equation [42]. In this model, the top-of-atmosphere antiproton flux $\Phi_{\bar{p}}^{\rm TOA}$ is obtained as

$$\frac{\Phi_{\bar{p}}^{\rm TOA}(E_{\bar{p}}^{\rm TOA})}{\Phi_{\bar{p}}^{\rm IS}(E_{\bar{p}}^{\rm IS})}=\left(\frac{p^{\rm TOA}}{p^{\rm IS}}\right)^2 \tag{21}$$

where E and p denote the total energies and momenta of interstellar and TOA antiprotons, which are related by the energy shift

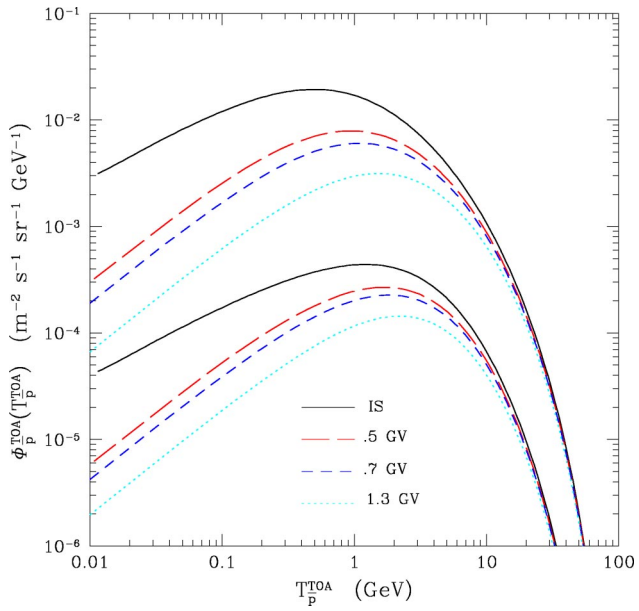

FIG. 13. Top-of-atmosphere antiproton fluxes as a function of the antiproton kinetic energy for the $m_\chi = 100$ GeV reference case. The upper (lower) set of curves refers to the maximal (minimal) set of astrophysical parameters. Solid curves show the interstellar fluxes. Broken curves show the effect of solar modulation at different periods of solar activity: $\phi = 500$ MV (long dashed), $\phi = 700$ MV (short dashed), and $\phi = 1300$ MV (dotted).

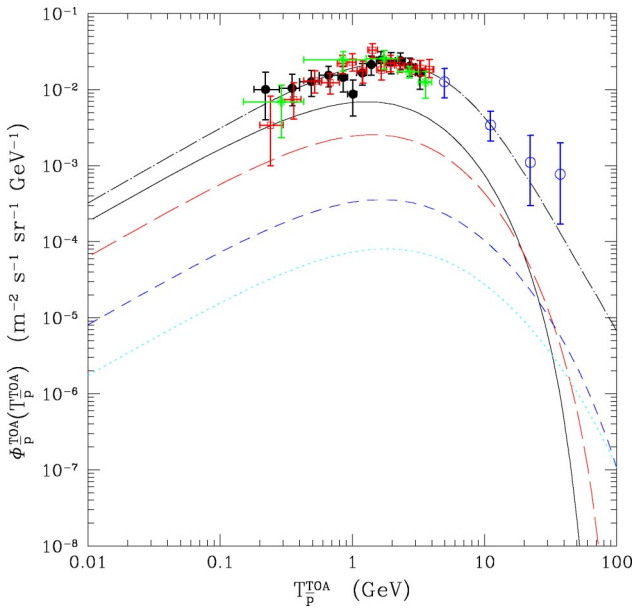

FIG. 14. Primary TOA antiproton fluxes as a function of the antiproton kinetic energy, for the representative spectra of Fig. 6 in the EMSSM. The solid line refers to $m_\chi = 60$ GeV, the long dashed line to $m_\chi = 100$ GeV, the short dashed line to $m_\chi = 300$ GeV, and the dotted line to $m_\chi = 500$ GeV. The astrophysical parameters correspond to the median choice. Solar modulation is calculated for a period of minimal solar activity. The upper dot dashed curve corresponds to the antiproton secondary flux taken from Refs. [18,28]. Full circles show the BESS 1995–1997 data [43]; the open squares show the BESS 1998 data [44]; the stars show the AMS data [46]; and the empty circles show the CAPRICE data [47].

$$E_{\bar{p}}^{IS} = E_{\bar{p}}^{IS} - \phi, \tag{22}$$

where the parameter ϕ is determined by fits on cosmic ray data. In our analysis, we will adopt the value $\phi = 500$ MV for periods of minimal solar activity, corresponding to the years around 1995–1998, $\phi = 700$ and $\phi = 1300$ MV for a transient period and for the solar maximum, respectively, which will be used for years 1999 and 2000.

Figure 13 shows the TOA antiproton fluxes for the $m_\chi = 100$ GeV reference configuration and for the maximal and minimal sets of astrophysical parameters. The figure shows that solar modulation has the effect of depleting the low-energy tail of the antiproton flux. The effect is clearly more pronounced for periods of strong solar activity, when the solar wind is stronger.

Data on antiprotons at the Earth are now abundant, mostly after the missions of the balloon-borne detector BESS. This experiment has provided measurements at different periods of solar activity [43–45]. It has now collected more than 2000 antiprotons between 200 MeV and 4 GeV. Data at solar minimum were also taken by the AMS experiment on board the shuttle [46] in an energy range similar to BESS, and by the CAPRICE balloon at higher energies, namely, between 5 GeV and 40 GeV [47]. All the data at solar minimum are plotted in Fig. 14 along with the secondary reference flux (for details, see Ref. [18]) and our predictions for primary fluxes at different neutralino masses in the EMSSM: $m_\chi = 60,100,300,500$ GeV and for the median set of astrophysical parameters. We notice that the primary flux from neutralino annihilation is at most of the same order of magnitude as the secondary flux, and this occurs for neutralino masses close to their current lower bound in the EMSSM, which is around $m_\chi \simeq 50$ GeV. We recall that the representative supersymmetric configurations plotted in Fig. 14 refer to a large antiproton production for each mass (i.e., they correspond to large values of the Υ parameter shown in Fig. 1). This indicates that the antiproton signal for neutralino dark matter will hardly produce an excess over the secondary flux, for an isothermal matter profile of the galactic halo and for $\rho_l = 0.3$ GeV cm^{-3}. This occurs for the median (and best) choice of the astrophysical parameters which govern the diffusion and propagation of antiprotons in the galaxy. Clearly, the maximal set of astrophysical parameters, which produces fluxes about one order of magnitude larger than the median set, may produce a large excess, for neutralino masses below 100–200 GeV. This excess could then be used to constrain supersymmetric models since the secondary flux is perfectly compatible with the data. However, for setting constraints on supersymmetry in a conservative way, we should instead use the set of astrophysical parameters which produces the minimal fluxes. In this case, the primary fluxes are lower than the ones plotted in Fig. 14 by about one order of magnitude, as discussed in the previous section. In conclusion, our analysis shows that, due to the large uncertainties in the primary fluxes, the antiproton signal is not suitable at present for setting *conservative* constraints on supersymmetric models. For this we need a better knowledge of the astrophysical

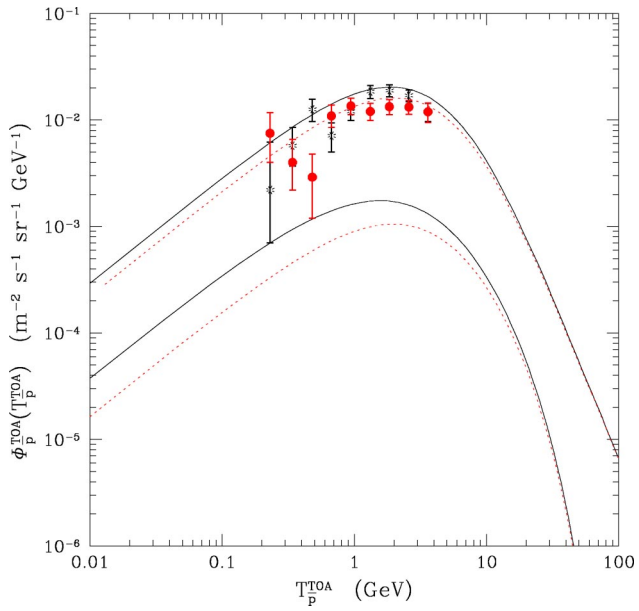

FIG. 15. Primary TOA antiproton fluxes at solar maximum for the transient periods of solar activity of the years 1999 and 2000. The upper set of curves shows the antiproton secondary fluxes. The lower set of curves shows the primary antiproton fluxes obtained for the representative $m_\chi = 100$ GeV case. The solar modulation parameter is fixed at 700 MV (solid lines) and at 1300 MV (dotted lines). The astrophysical parameters correspond to the median case. Stars and full circles correspond to BESS 1999 and 2000, respectively [45].

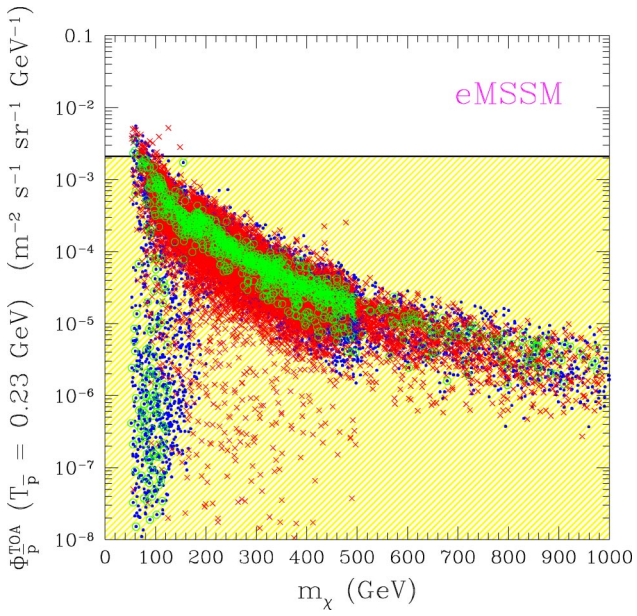

FIG. 16. (Color online) Antiproton flux at solar minimum from neutralino annihilation calculated at $T_{\bar{p}} = 0.23$ GeV, as a function of the neutralino mass for a generic scan of the EMSSM. The flux is calculated for a smooth halo described by an isothermal profile with core radius $a = 3.5$ kpc and for the median set of astrophysical parameters. Crosses (red) refer to cosmologically dominant neutralinos ($0.05 \leqslant \Omega_\chi h^2 \leqslant 0.3$); dots (blue) refer to subdominant relic neutralinos ($\Omega_\chi h^2 < 0.05$); light circles (in green) show the EMSSM configurations for which the neutralino relic abundance lies in the preferred range for CDM, as determined by the combined WMAP + 2DFGRS + Lyman-α analysis: $0.095 \leqslant \Omega_{\rm CDM} h^2 \leqslant 0.131$ [1]. The shaded region (yellow) denotes the amount of antiprotons, in excess of the secondary component [18], which can be accommodated at $T_{\bar{p}} = 0.23$ GeV in order not to exceed the observed flux, as measured by BESS [43,44]. All the points of the scatter plot that lie below the horizontal black line are compatible with observations.

parameters that govern the diffusion and propagation of primary antiprotons in the galaxy.

Antiproton data are also available for periods of intense solar activity from the BESS detector. Figure 15 shows these data together with the secondary flux and the primary flux calculated for the representative $m_\chi = 100$ GeV configuration. The astrophysical parameters are fixed at their median values. We see that at solar maximum also the secondary flux is compatible with the data and the supersymmetric flux is remarkably smaller than the secondary one.

In our discussion so far, we have commented that *conservative* and solid constraints on supersymmetric models require the use of the minimal set of astrophysical parameters. This attitude is needed in setting limits. However, the best and most probable choice of astrophysical parameters is the median one, and we will therefore adopt from here on this set of parameters for our analyses. It is likely that a sharpening of the knowledge of the propagation parameters will lead to a shrinking of the allowed uncertainty band around the central (median) value.

In order to compare the experimental results with a full scan of the supersymmetric parameter space, we calculate the TOA antiproton fluxes in two different energy bins and compare our results with the excess which can be accommodated above the secondary flux in order not to enter into conflict with the experimental data in that energy bin. We have chosen a low-energy bin $T_{\bar{p}} = 0.23$ GeV, and a high-energy one $T_{\bar{p}} = 37.5$ GeV. As can be seen in Fig. 14, in the low-energy bin the secondary flux is perfectly compatible with the data, therefore no excess is needed: this allows us to set an upper bound on the possible amount of antiprotons of primary origin which can be accommodated: $\Phi_{\bar{p}}^{\rm TOA}(T_{\bar{p}} = 0.23\ {\rm GeV}) \lesssim 2.09 \times 10^{-3}\ {\rm m}^{-2}\,{\rm s}^{-1}\,{\rm sr}^{-1}\,{\rm GeV}^{-1}$. This value is obtained by taking into account the values and uncertainties of both data and secondary flux at $T_{\bar{p}} = 0.23$ GeV. At $T_{\bar{p}} = 37.5$ GeV, even though the data and the secondary flux are statistically compatible, a possible excess may be accommodated, since the central value of the experimental point indicates a much larger flux as compared to the secondary component. In this case, we can define an interval of values for a possible excess: $0.04 \times 10^{-3} \lesssim \Phi_{\bar{p}}^{\rm TOA}(T_{\bar{p}} = 37.5\ {\rm GeV}) \lesssim 1.87 \times 10^{-3}$ in units of ${\rm m}^{-2}\,{\rm s}^{-1}\,{\rm sr}^{-1}\,{\rm GeV}^{-1}$. We compare these intervals with our calculations in the EMSSM and in MSUGRA.

Figure 16 shows the scatter plot of the antiproton flux calculated at $T_{\bar{p}} = 0.23$ GeV for a generic scan of the EMSSM scheme. The supersymmetric fluxes are clearly largest at low neutralino masses, and they decrease as the neutralino mass increases mostly because the neutralino number density in the galaxy scales as m_χ^{-2}. A small fraction of configurations with masses below 100 GeV can provide

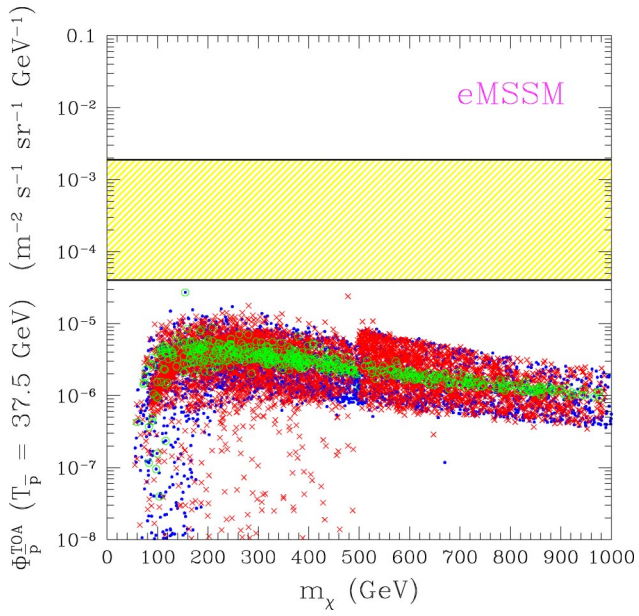

FIG. 17. Antiproton flux at solar minimum from neutralino annihilation calculated at $T_{\bar{p}}=37.5$ GeV, as a function of the neutralino mass for a generic scan of the EMSSM. Notations are as in Fig. 16. The shaded region (in yellow) denotes the amount of antiprotons which would be required at $T_{\bar{p}}=37.5$ GeV in order to explain the possible excess in the BESS data [43,44] over the secondary component [18]. All the points of the scatter plot that lie below the upper horizontal black line are compatible with observations.

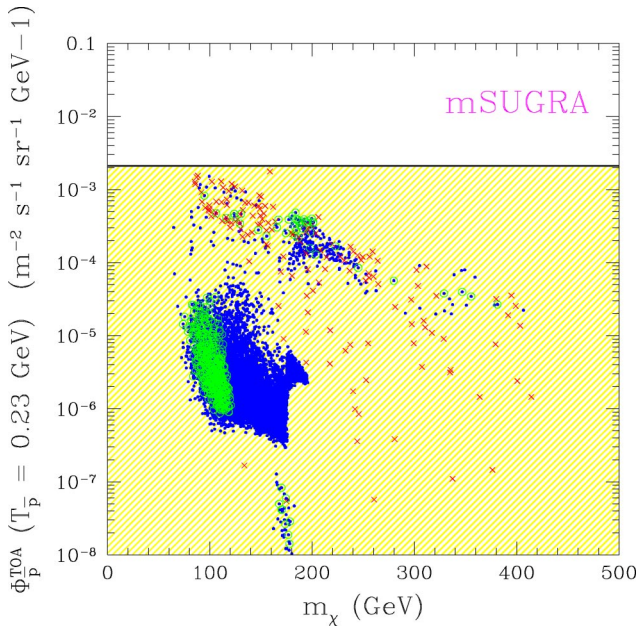

FIG. 18. The same as in Fig. 16, for a generic scan of the MSUGRA scheme.

fluxes which could be potentially at the edge of producing an excess, but we recall here that for a safe exclusion of these configurations we should use the minimal set of astrophysical parameters, which provides a flux that is about one order of magnitude smaller. In any case, a reduction of the uncertainties on the primary flux calculation and a future reduction of experimental errors may eventually allow one either to set limits to supersymmetry or to show a positive excess of antiprotons in this low-energy bin, a fact which could then be explained as originated by neutralinos of masses below 100 GeV. Figure 17 shows the scatter plot of the antiproton flux calculated at $T_{\bar{p}}=37.5$ GeV for the same scan of the EMSSM. In this case we observe that all the supersymmetric configurations are compatible with data, but there are no supersymmetric models that allow us to explain the discrepancy between the data and the secondary flux as due to an excess of supersymmetric origin.

The situation in the MSUGRA scheme is shown in Fig. 18 with the flux of antiprotons at $T_{\bar{p}}=0.23$ GeV. In this case, as already observed in connection with the properties of the MSUGRA source term, the antiproton fluxes are smaller than in the EMSSM case. Nevertheless, a restricted fraction of MSUGRA configuration is potentially explorable in the future, with a reduction of the experimental error of about a factor of 2–3.

The fluxes we have shown so far all refer to a dark matter density distribution in the form of a cored isothermal sphere. Clearly, a halo profile that is able to produce an overdensity with respect to the isothermal sphere would produce a larger antiproton flux. We can parameterize the enhancement of the matter density by a multiplicative factor η, which then enters as η^2 in the calculation of the antiproton primary flux, since the flux depends on the square of the matter density. The origin of the overdensity may be due, for instance, to flattening of the galactic halo or to the presence of clumps. It the latter case, the enhancement factor is likely to be smaller than about 5, once the results of Ref. [41] are implemented with our discussion on the antiproton diffusion region in the galaxy. The enhancement factor may also be related to a different choice of the local dark matter density, which has been fixed at $\rho_l=0.3$ GeV cm^{-3} in our analysis. We recall that our cored isothermal sphere allows factors of η up to $\eta\sim(0.71/0.3)=2.4$ [21]. Clearly, a complete reanalysis of the propagation and diffusion properties will be required for each different choice of the halo shape: this reanalysis will give the amount of enhancement concerning the specific halo. In any case, regardless of how the enhancement η is obtained, we can discuss the effect of such an increased flux by using η as a normalization factor to show the amount of enhancement which is required in order to interpret the antiproton excess at $T_{\bar{p}}=37.5$ GeV as due to neutralino dark matter, without exceeding the upper limit on the antiproton flux at $T_{\bar{p}}=0.23$ GeV. Figure 19 shows the correlation between the EMSSM antiproton fluxes at $T_{\bar{p}}=0.23$ GeV and $T_{\bar{p}}=37.5$ GeV for $\eta=3$ and 10. The supersymmetric configurations which could satisfy this requirement are the ones that fall inside the shaded area in Fig. 19. We see that the possible excess at $T_{\bar{p}}=37.5$ GeV requires halo overdensities of at least a factor of 2–3 and neutralino masses larger than a few hundreds of GeV. This last property is simply understood on the basis of the fluxes shown in Fig. 14: the phase space cutoff at $T_{\bar{p}}=m_\chi$ implies that a light neutralino would need a huge overdensity factor in order to match the observed antiproton flux at $T_{\bar{p}}=37.5$ GeV, but this would produce an exceedingly large flux at $T_{\bar{p}}=0.23$ GeV. On the

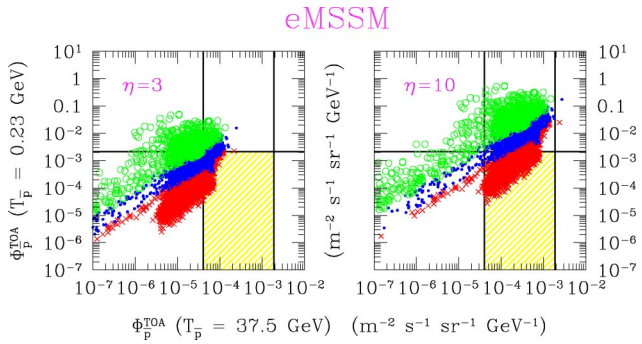

FIG. 19. (Color online) Correlation between the antiproton flux at $T_{\bar{p}}=0.23$ GeV and $T_{\bar{p}}=37.5$ GeV shown in Figs. 16 and 17 for the astrophysical enhancement parameter $\eta=3$ and 10 (overdense halos) and for the median set of astrophysical parameters. Circles (green), dots (blue), and crosses (red) denote configurations with neutralino masses in the ranges 50 GeV$<m_\chi<$150 GeV, 150 GeV$<m_\chi<$300 GeV, and 300 GeV$<m_\chi<$1 TeV, respectively. The horizontal line denotes the upper limit on the antiproton flux at $T_{\bar{p}}=0.23$ GeV coming from the BESS data [43,44], once the secondary component [18] is taken into account. The rightmost vertical line denotes the corresponding upper limit at $T_{\bar{p}}=37.5$ GeV. The shaded area indicates configurations which can explain the possible excess in the data [43,44] over the secondary component [18] at $T_{\bar{p}}=37.5$ GeV, without giving an excess at low kinetic energies ($T_{\bar{p}}=0.23$ GeV).

contrary, heavy neutralinos have a phase space cutoff at much higher kinetic energies, and therefore a mild overdensity may enhance the flux at $T_{\bar{p}}=37.5$ GeV without giving conflict at low kinetic energies.

VI. CONCLUSIONS AND PERSPECTIVES

We have calculated the flux of antiprotons produced by relic neutralino annihilations in the galactic halo in a detailed diffusion model constrained by analysis of stable and radioactive nuclei. The source of antiprotons is studied both in a low-energy minimal supersymmetric standard model and in a supergravity-inspired supersymmetric scheme. We find that the interstellar primary antiproton fluxes are affected by a large uncertainty, which spans two orders of magnitude at low antiproton kinetic energies. This is at variance with the secondary antiproton fluxes (whose uncertainty never exceeds 24% [19]) and it is mainly related to the fact that the source of the primary flux is located inside the diffusive halo, whose size is unknown. By adopting a conservative choice for the dark matter density profile and propagation parameters, no supersymmetric configuration can be excluded on the basis of an excess over the existing data. Actually, the data are quite well explained by the secondary contribution alone. However, if we adopt the best values for the propagation parameters (corresponding to a thickness of the diffusive halo of 4 kpc), a window of low-mass neutralino configurations provides fluxes which, once summed up to the secondary contribution, are in excess of the experimental measurements. We have shown that the sensitivity to the antiproton signal is increased with the halo size and limited by strong convection. An improved knowledge of the propagation parameters will certainly help in reducing the uncertainty on the primary flux and consequently it could allow us to set more severe constraints on the supersymmetric parameter space.

The sensitivity of the primary antiproton flux to the shape of the dark matter density profile has also been investigated. We have shown that the shape of the dark matter density distribution does not introduce large uncertainties. In particular, we have demonstrated that a NFW distribution can increase the primary antiproton flux by no more than 20% with respect to the isothermal profile. Indeed, it is very improbable to detect at the Earth antiprotons produced in the central regions of the galaxy, where the two distributions differ most.

In future years several balloon-borne experiments such as BESS, space-based detectors such as AMS, and satellites such as PAMELA will provide very abundant and accurate data on the antiproton flux. At the same time, new data on cosmic-ray nuclei are expected and would lead to a better knowledge of the cosmic-ray propagation mechanisms. We could thus expect a dramatic reduction of the uncertainties affecting the neutralino-induced antiproton flux, and much more definite predictions for antiprotons of supersymmetric origin will then be possible. Much effort is also devoted to other indirect neutralino searches, such as positrons and antideuterons in cosmic rays, gamma rays, and up-going muons, as well as to direct searches in deep underground laboratories, thus giving the hope that a more constraining analysis on the existence of relic neutralinos in the halo of our galaxy will be viable.

ACKNOWLEDGMENTS

We warmly thank Professor A. Bottino for very useful discussions. N.F. wishes to acknowledge the warm hospitality and support of the Korean Institute for Advanced Study (KIAS), where part of this work was done.

APPENDIX A: CALCULATION OF THE ANTIPROTON DIFFERENTIAL SPECTRUM PER ANNIHILATION EVENT

The antiproton differential spectrum per annihilation event $g(T_{\bar{p}})$ is calculated by following analytically the decay chain of the neutralino annihilation products until a quark or a gluon h is produced. The antiproton spectrum is then obtained by a Monte Carlo modeling of the quark and gluon hadronization (we make use of the PYTHIA package [24]). We have produced the $\bar{p}$ differential distributions for an $h=u,d,s,c,b$ gluon at various injection energies for each h (the t quark is assumed to decay before hadronization and is treated analytically, since in addition to its standard model decay into W^+b, it may have a supersymmetric decay into H^+b). Whenever we need the $\bar{p}$ distribution for an injection energy different from the ones produced, we perform an interpolation. In order to obtain the antiproton differential distribution in the neutralino rest frame we perform the necessary boosts on the MC spectra.

For instance, let us consider a $\bar{p}$ production from a neu-

tralino decay chain of this type:

$$\chi\chi \to A \to a \to h \rightsquigarrow \bar{p}. \tag{A1}$$

The antiproton differential spectrum per annihilation event $g(T_{\bar{p}})$ is then obtained by the product of the branching ratios for the production of A, a, and h in the decay chain, with the differential distribution of antiprotons produced by the hadronization of an h injected at an energy $E_{\rm prod}$ (defined in the rest frame of the a decaying particle) double boosted to the χ reference frame:

$$g(T_{\bar{p}}) = \mathrm{BR}(\chi\chi \to A)\mathrm{BR}(A \to a)\mathrm{BR}(a \to h) \times \left[\left(\frac{dN_{\bar{p}}^{h}}{dT_{\bar{p}}} \right)_{\text{boost } a \to A} \right]_{\text{boost } A \to \chi}. \tag{A2}$$

The first boost transforms the spectrum from the rest frame of a (in which h is injected with energy $E_{\rm prod}$) to the rest frame of A. The second brings the distribution to the rest frame of χ. Each boost is obtained by the following expression:

$$g(E_{\bar{p}}) = \frac{1}{2} \int_{E'_-}^{E'_+} \left(\frac{dN_{\bar{p}}^{h}}{dE'} \right) \Bigg|_{E_{\rm prod}} \frac{dE'}{\gamma\beta p'} \tag{A3}$$

where $E_{\bar{p}} = T_{\bar{p}} + m_{\bar{p}}$ is the total antiproton energy, $p' = \sqrt{(E'^2 + m_{\bar{p}}^2)}$, γ and β are the Lorentz factors of the boost, and the interval of integration is defined by

$$E'_{\pm} = \min\left[E_{\rm prod}, \gamma E_{\bar{p}} \left(1 \pm \beta \sqrt{1 - \frac{m_{\bar{p}}^2}{E_{\bar{p}}^2}} \right) \right]. \tag{A4}$$

APPENDIX B: SOLUTION OF THE DIFFUSION EQUATION

In cylindrical geometry, the differential density $N^{\bar{p}}(r,z,E)$ is given by

$$0 = \left\{ K(E) \left[\frac{\partial^2}{\partial z^2} + \frac{1}{r} \frac{\partial}{\partial r} \left(r \frac{\partial}{\partial r} \right) \right] - V_c \frac{\partial}{\partial z} \right\} N^{\bar{p}}(r,z,E) + \mathcal{Q}^{\bar{p}}(r,z,E) - 2h\,\delta(z)\Gamma^{\bar{p}}(E) N^{\bar{p}}(r,z,E), \tag{B1}$$

where the energy losses have been omitted, for the sake of clarity. The source term includes primary antiprotons, from exotic sources present in the dark halo, annihilating throughout the diffusive halo of the galaxy, and secondary antiprotons, standard p and He CR's spallating on the interstellar gas in the thin disk, and may be written as

$$\mathcal{Q}^{\bar{p}}(r,z,E) = q^{\bar{p},\rm prim}(r,z,E) + 2h\,\delta(z) q^{\bar{p},\rm sec}(r,0,E). \tag{B2}$$

A convenient way to solve Eq. (B1) is to expand all the functions $f(r)$ [the density $N(r)$ and the source distribution $q(r)$] that depend on r on the orthogonal set of Bessel functions $\{J_0(\zeta_i x)\}^{i=1,\ldots,\infty}$ (where ζ_i are the zeros of J_0). These Bessel transforms are defined as

$$f(r) = \sum_{i=1}^{\infty} f_i J_0\left(\zeta_i \frac{r}{R} \right), \tag{B3}$$

with

$$f_i = \frac{2}{J_1^2(\zeta_i)} \int_0^1 \rho f(\rho R) J_0(\zeta_i \rho) d\rho. \tag{B4}$$

Using the Fourier-Bessel coefficients $N_i^{\bar{p}}(z,E)$ and $q_i^{\bar{p}}(z,E)$, there is no conceptual difficulty to extract solutions of Eq. (B1). We do not repeat the derivation, which can be a bit lengthy. Solutions for primaries can be found in Ref. [14], whereas the one for secondaries has been discussed in Ref. [18].

1. Energy losses, tertiary component

Following the procedure described, e.g., in Ref. [19], energy losses and diffusive reacceleration lead to a differential equation on $N_i(z=0,E)$:

$$A_i N_i(0,E) = \mathcal{Q}_i(E) - 2h \frac{\partial}{\partial E} \left\{ b_{\rm loss}(E) N_i(0,E) - K_{EE} \frac{\partial N_i(0,E)}{\partial E} \right\}, \tag{B5}$$

where $b_{\rm loss} = b_{\rm ion} + b_{\rm Coul} + b_{\rm adiab}$ includes the three kinds of energy losses. The exact forms for these terms may be found in Refs. [19,28]. The resolution of this equation proceeds as described in Appendixes A.2, A.3, and B of Ref. [18], to which we refer for further details. The source term also takes into account the so-called tertiary component $q_i^{\rm ter}(E)$, corresponding to an inelastic but nonannihilating reaction of $\bar{p}$ on interstellar matter. This mechanism merely redistributes antiprotons toward lower energies and tends to flatten their spectrum.

[1] WMAP Collaboration, C.L. Bennett *et al.*, Astrophys. J., Suppl. Ser. **148**, 1 (2003); WMAP Collaboration, D.N. Spergel *et al.*, *ibid.* **148**, 175 (2003).

[2] Supernova Cosmology Project Collaboration, S. Perlmutter *et al.*, Astrophys. J. **517**, 565 (1999).

[3] W.J. Percival *et al.*, Mon. Not. R. Astron. Soc. **327**, 1297 (2001).

[4] S. Burles and D. Tytler, Astrophys. J. **499**, 699 (1998); **507**, 732 (1998); R.H. Cyburt, B.D. Fields, and K.A. Olive, Phys. Lett. B **567**, 227 (2003).

[5] L. Bergström, Rep. Prog. Phys. **63**, 793 (2000); A. Morales, in *VII Workshop on Topics in Astroparticle and Underground*

Physics (TAUP 2001), Gran Sasso, Italy, 2001 [Nucl. Phys. B (Proc. Suppl.) **110,** 39 2002], J. Ellis, in IV International Heidelberg Conference on Dark Matter in Astro and Particle Physics; Cape Town, South Africa, 2002, astro-ph/0204059; A. Bottino and N. Fornengo, in Fifth School on Non-Accelerator Particle Astrophysics, ICTP, Trieste, 1998, hep-ph/9904469.

[6] EDELWEISS Collaboration, A. Benoit *et al.*, Phys. Lett. B **545**, 43 (2002); CDMS Collaboration, D. Abrams *et al.*, Phys. Rev. D **66**, 122003 (2002); DAMA/NaI Collaboration, R. Bernabei *et al.*, Phys. Lett. B **389**, 757 (1996); Riv. Nuovo Cimento **26**, 1 (2003) and references therein.

[7] A. Bottino, F. Donato, N. Fornengo, and S. Scopel, Phys. Rev. D **63**, 125003 (2001).

[8] R. Arnowitt, B. Dutta, B. Hu, and Y. Santoso, Phys. Lett. B **505**, 177 (2001); J. Ellis, A. Ferstl, K.A. Olive, and Y. Santoso, Phys. Rev. D **67**, 123502 (2003); V.A. Bednyakov and H.V. Klapdor-Kleingrothaus, *ibid.* **63**, 095005 (2001); Y.G. Kim, T. Nihei, L. Roszkowski, and R. Ruiz de Austri, J. High Energy Phys. **12**, 034 (2002); A. Bottino, F. Donato, N. Fornengo, and S. Scopel, Phys. Rev. D **62**, 056006 (2000); Astropart. Phys. **13**, 215 (2000).

[9] A. Bouquet, P. Salati, and J. Silk, Phys. Rev. D **40**, 3168 (1989); H.U. Bengtsson, P. Salati, and J. Silk, Nucl. Phys. **B346**, 129 (1990); L. Bergstrom, P. Ullio, and J. Buckley, Astropart. Phys. **9**, 137 (1998).

[10] E.A. Baltz, C. Briot, P. Salati, R. Taillet, and J. Silk, Phys. Rev. D **61**, 023514 (2000).

[11] HEGRA Collaboration, F. Aharonian *et al.*, Astron. Astrophys. **403**, L1 (2003).

[12] HEAT Collaboration, S. Coutu *et al.*, Astropart. Phys. **11**, 429 (1999).

[13] A. Bottino, F. Donato, N. Fornengo, and P. Salati, Phys. Rev. D **58**, 123503 (1998).

[14] A. Barrau, G. Boudoul, F. Donato, D. Maurin, P. Salati, and R. Taillet, Astron. Astrophys. **388**, 376 (2002).

[15] L. Bergström, J. Edsjö, and P. Ullio, Astrophys. J. **526**, 215 (1999).

[16] F. Donato, N. Fornengo, and P. Salati, Phys. Rev. D **62**, 043003 (2000); P. Chardonnet, J. Orloff, and P. Salati, Phys. Lett. B **409**, 313 (1997).

[17] A. Barrau, G. Boudoul, F. Donato, D. Maurin, P. Salati, I. Stefanon, and R. Taillet, Astron. Astrophys. **398**, 403 (2003).

[18] F. Donato, D. Maurin, P. Salati, A. Barrau, G. Boudoul, and R. Taillet, Astrophys. J. **563**, 172 (2001).

[19] D. Maurin, F. Donato, R. Taillet, and P. Salati, Astrophys. J. **555**, 585 (2001).

[20] A. Bottino, C. Favero, N. Fornengo, and G. Mignola, Astropart. Phys. **3**, 77 (1995).

[21] P. Belli, R. Cerulli, N. Fornengo, and S. Scopel, Phys. Rev. D **66**, 043503 (2002).

[22] V. Berezinsky, A. Bottino, J. Ellis, N. Fornengo, G. Mignola, and S. Scopel, Astropart. Phys. **5**, 1 (1996); **5**, 333 (1966).

[23] J.L. Feng, K.T. Matchev, and F. Wilczek, Phys. Lett. B **482**, 388 (2000).

[24] T. Sjöstrand *et al.*, Comput. Phys. Commun. **135**, 238 (2001).

[25] A. Bottino, V. de Alfaro, N. Fornengo, G. Mignola, and M. Pignone, Astropart. Phys. **2**, 67 (1994).

[26] A. Bottino, N. Fornengo, and S. Scopel, Phys. Rev. D **67**, 063519 (2003).

[27] A. Bottino, F. Donato, N. Fornengo, and S. Scopel, Phys. Rev. D **68**, 043506 (2003).

[28] D. Maurin, R. Taillet, F. Donato, P. Salati, A. Barrau, and G. Boudoul, *Recent Developments in Astrophysics* (in press), astro-ph/0212111.

[29] E.S. Seo and V.S. Ptuskin, Astrophys. J. **431**, 705 (1994).

[30] D. Maurin, R. Taillet, and F. Donato, Astron. Astrophys. **394**, 1039 (2002).

[31] F. Donato, D. Maurin, and R. Taillet, Astron. Astrophys. **381**, 539 (2002).

[32] R. Taillet and D. Maurin, Astron. Astrophys. **402**, 971 (2003); D. Maurin and R. Taillet, *ibid.* **404**, 949 (2003).

[33] F.C. Jones, Astrophys. J. **222**, 1097 (1978).

[34] A.W. Strong and I.V. Moskalenko, Astrophys. J. **509**, 212 (1998).

[35] I.V. Moskalenko, A.W. Strong, J.F. Ormes, and S.G. Mashnik, Astrophys. J. **586**, 1050 (2003).

[36] R. Taillet, P. Salati, D. Maurin, E. Vangioni-Flam, and M. Cassé, astro-ph/0308141.

[37] S. Ghigna, B. Moore, F. Governato, G. Lake, T. Quinn, and J. Stadel, Astrophys. J. **544**, 616 (2000).

[38] J.F. Navarro, C.S. Frenk, and S.D.M. White, Astrophys. J. **490**, 493 (1997).

[39] W. Dehnen and J. Binney, Mon. Not. R. Astron. Soc. **294**, 429 (1998).

[40] R.P. Olling and M.R. Merrifield, Mon. Not. R. Astron. Soc. **326**, 164 (2001).

[41] V. Berezinsky, V. Dokuchaev, and Yu. Eroshenko, Phys. Rev. D **68**, 103003 (2003).

[42] J.S. Perko, Astron. Astrophys. **184**, 119 (1987).

[43] BESS Collaboration, S. Orito *et al.*, Phys. Rev. Lett. **84**, 1078 (2000).

[44] BESS Collaboration, T. Maeno *et al.*, Astropart. Phys. **16**, 121 (2001).

[45] BESS Collaboration, Y. Asaoka *et al.*, Phys. Rev. Lett. **88**, 051101 (2001).

[46] AMS Collaboration, M. Aguilar *et al.*, Phys. Rep. **366**, 331 (2002).

[47] CAPRICE Collaboration, M. Boezio *et al.*, Astrophys. J. **561**, 787 (2001).